Self-Optimizing Metamaterial Antennas

Mikala C. Johnson

A dissertation
submitted in partial fulfillment of the
requirements for the degree of

Doctor of Philosophy

University of Washington

2014

Reading Committee:

Jose Nathan Kutz, Chair

Nathan B. Kundtz

Steven L. Brunton

Emanuil V. Todorov

Program Authorized to Offer Degree:
Applied Mathematics

University of Washington

Abstract

Self-Optimizing Metamaterial Antennas

Mikala C. Johnson

Chair of the Supervisory Committee:
Chair and Professor Jose Nathan Kutz
Department of Applied Mathematics

The reconfigurable holographic metamaterial antenna is an attractive new technology for satellite communications, particularly in mobile applications. This antenna is thin, lightweight, consumes little power to operate, and is inexpensive to manufacture. Yet, perhaps its most promising attribute is software-controlled beam steering - this antenna does not require moving parts and is still able to receive or transmit data without interruption to a moving, non-geosynchronous satellite (for example, a satellite in low Earth orbit, medium Earth orbit, or highly elliptic orbit), from a moving platform (for example, a plane, ship, or automobile), or both. However, the antenna cannot achieve continuous, high performance operation without robust, adaptive optimal pattern synthesis. Yet, as the antenna hardware is new and under development, so also has the adaptive software control aspect not been developed.

This thesis derives and demonstrates an effective adaptive control approach to manage and improve the beam pattern of the reconfigurable holographic metamaterial antenna (RHMA) continuously during operation when deployed. This approach is developed in three steps. First, a computational model of the antenna that accurately predicts the antenna response is derived and validated to study the RHMA's behavior and experiment with synthesis of patterns. Second, a pattern synthesis approach that cancels sidelobes that typically occur in the RHMA's radiation pattern is designed and proven effective both computation-

ally and experimentally. Finally, an adaptive controller is added to the pattern synthesis, which enables continuous automatic, robust control of the RHMA even in the presence of measurement error and changing environmental conditions.

Altogether, the work in this thesis significantly advances the demonstrated capabilities of the RHMA. This thesis is the first work that not only theoretically explores pattern synthesis of the RHMA, but then designs and implements a viable adaptive controller for self-optimizing beam pattern control. The algorithmic infrastructure demonstrated in this work meets the dynamic operational requirements of the RHMA, and as an overall algorithmic package, the mathematical framework provides a robust, machine-intelligent architecture capable of enabling the RHMA technology.

TABLE OF CONTENTS

LIST OF FIGURES

ACKNOWLEDGMENTS

I wish to express my sincere appreciation to my adviser(s) and committee for guidance in the pursuit of this research. I am particularly grateful to my primary adviser at the time of this thesis and final defense Nathan Kutz and Steve Brunton. Their time and attention have meant the difference between "interesting" work and "meaningful" or "significant" work. I also would like to extend my gratitude to all the professors and teachers who challenged me throughout the years. I also thank my friends and colleagues for patience, support, and assistance through the drudgery of this effort.

Mine has not been the common (though there is no "normal") Ph.D. path. The change of fortune that occurred by taking an internship offered by my now-committee member Nathan Kundtz after finding myself adviser-less at the end of my fourth year of graduate work was momentous. This brief internship led me to a new project in both of the exciting and ever-more rapidly advancing fields of metamaterials and machine-intelligent control. I thank Kymeta (the metamaterial antenna start-up) for supporting this Ph.D. work both professionally with many resources, not the least of which was a whole host of colleagues that aided this work, but also personally with the interest and support of the management of the company.

I am also deeply thankful for my parents and extended family for their decades of support and encouragement of my eduction. Finally, I wish to express a special gratitude for the support proffered and redoubled every day by my companion Tom throughout the last, most-intensive year, which saw the writing of three journal articles, several conference proceedings, my general exam, this thesis, and the final exam. Thank you.

Chapter 1

INTRODUCTION

1.1 Motivation

A material which is engineered to obtain controllable electromagnetic response characteristics is commonly referred to as a *metamaterial*. Metamaterials are comprised of unit cells, or elements, in the way that a classical material is comprised of molecules though the metamaterial unit cell is itself a macroscopic structure. A metamaterial is a collection, typically an ordered two or three dimensional array, of unit cells. Yet, it is the collective behavior of all the cells that gives the metamaterial its startling, non-natural electromagnetic response. The most well-known characteristic achieved by the engineering of metamaterials is simultaneous negative magnetic permeability and electric permittivity [1], and metamaterials were responsible for the successful experimental demonstration of the celebrated application of electromagnetic cloaking in 2006 [2].

Yet, there are many other applications in which engineering the electromagnetic response of a material is useful, and, indeed, many other applications that are easier to achieve than the Harry Potter-esque invisibility cloak. For example, metamaterials are being designed to produce new imaging capabilities [3], phase-change materials for data storage [4], sound focusing materials [5], and new generation solar panels [6]. One area that has seen intensive development with the advent of metamaterials is antenna design. Metamaterials are enabling smaller, highly-directive antennas [7, 8] and novel architectures, for example, frequency selective surfaces [9] and a flat lens horn antenna [10]. The introduction of the reconfigurable holographic metamaterial antenna that is the subject of this thesis is poised to re-energize the satellite communications sector, particularly mobile applications (moving antenna platforms, moving satellites, or both).

Arthur C. Clark proposed the concept of geosynchronous satellites as communications relay platforms in October 1945 [11]. The promise of satellite communications was turned into reality with the launch of Sputnik in 1957. It then took until 1972 for this concept to find its way into commercial reality with the launch of Westar 1 in April 1974, the first U.S. domestic commercial communications satellite. Since that time the geosynchronous arc has been filling with hundreds of satellites providing television, data, internet, and other communications on a global scale. There has proven to be an ever-growing demand for ubiquitous wireless communications with ever-increasing bandwidths, at faster data rates, and with lower latency.

To address this evolving demand, the satellite industry is looking to leverage the potential of non-geosynchronous orbital (NGSO) architectures in addition to the proven geosynchronous, twenty-four hour, orbits. There will be new satellite constellations in a variety of lower orbits that will require a new generation of beamforming and tracking antennas to unlock the utility value of these alternative orbits that still provide universal coverage but at much lower latency. Presently, O3b, Globalstar, Iridium, PlanetLabs, PlanetIQ, and Skybox Imaging are exploiting various NGSO deployments. Three of these non-geosynchronous orbits are depicted in figure 1.1, and the representative achievable performance characteristics of these different constellations are given in table 1.1. A non-geosnynchronous orbit requires the antenna on the ground to be able to track the satellite as it moves across its field of vision. In parallel with the success of cell phones, laptops, and tablets, satellite communications consumers are also looking to be able to access data wherever they are, even while fully mobile. This means that the satellite industry is seeking satellite terminal solutions that can deliver connections continuously to aircraft, trains, buses, boats, automobiles, and individuals.

The fixed parabolic reflector antenna (frequently referred to as a "dish" antenna) is the mature technology that is ubiquitously used to transmit to and receive from the geostationary satellites. On the other hand, the mobile applications require a different antenna.

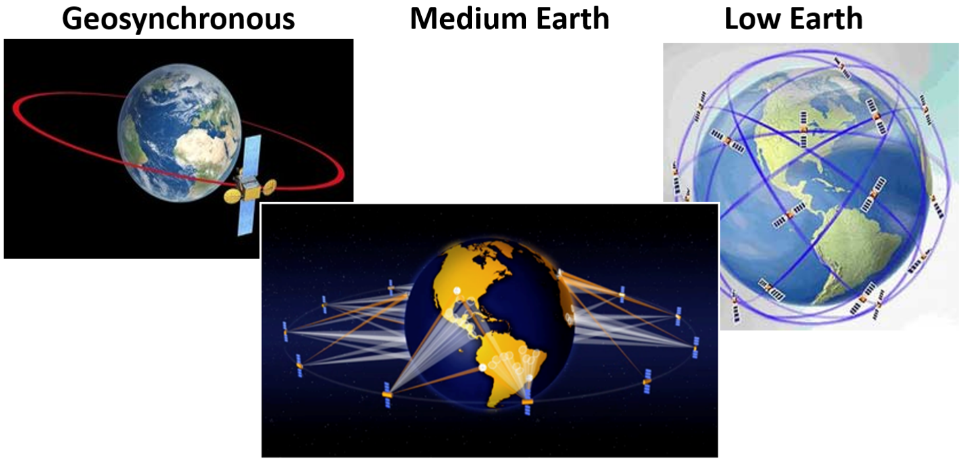

Figure 1.1: Visualization of various satellite orbits. (Left to right) Geosynchronous orbit, medium Earth orbit, low Earth orbit. At lower orbits, the satellites move with respect to the field of view of the ground terminal. This movement requires the ground antenna to be able to steer its beam to track the satellite.

The most obvious solution is to use the mature parabolic reflector antenna and mechanize it to be able to move; this is called a gimballed reflector. Gimballed reflectors require trained human intervention to be set up and they require frequent maintenance as their mechanical parts are susceptible to environmental impacts like corrosion; they are also heavy and bulky. Several gimballed dishes for a variety of mobile applications are shown in figure 1.2. To address the fundamentally different requirements of a mobile environment, a different type of technology has been more recently developed for satellite communications - the phased array. The phased array was developed at lower radio frequencies in 1905 by Karl Braun, but its electronic beamsteering advantage over the parabolic reflector when dynamic satellite communication was called for pushed the development of phased arrays to satellite communication frequencies [12]. Several pictures of phased arrays for satellite communications in current mobile applications are shown in figure 1.3. Phased arrays are advantageous because they may not require mechanical movement, instead relying on software-controlled beamforming, though it is notable from figure 1.3 that today's phased array technology for

Table 1.1: Performance characteristics of various satellite orbits

Parameter	GEO	MEO	LEO
Satellite height (km)	35,786	5,000-12,000	500-1,500
Orbital period (hours)	24	2-8	0.17-0.67
Num of satellites for global coverage	3	8-20	40-80
Hand-off requirements	None	Medium	Fast
2-way latency (ms)	500	120	**12**
Path Loss at 20 GHz (dB)	198.5	185.5	**164.4**
Data rates (Mbps)	10+	300+	**1000+**

commercial mobile applications still require some level of mechanical movement. Even these hybrid mechanical-phased array systems have not attained widespread use at satellite frequencies because they rely on individual antennas (typically horns or dipoles) to form the array along with phase-shifters (which may be active or passive), so they require high levels of power for operation, additional cooling, and they are expensive [13]. The metamaterial antenna solves all these problems - operating without physical movement through electronic reconfiguration like a phased array but without the attendant cost and power requirements. Figure 1.4 depicts several mobile applications of the metamaterial antenna, and table 1.2 is a collection of typical performance characteristics for the different varieties of antenna. The metamaterial antenna has significant physical advantages over the incumbent gimballed reflector and phased array antenna technologies.

The promise of metamaterial antennas to change the landscape of satellite communications is rooted in two related aspects. The first is its collective physical attributes, being thin, light-weight, low-power consuming, and cheap to manufacture. The other is its ability to beam steer through software - the intelligence, flexibility, robustness, and adaptability enabled when control of the antenna is seated in mathematical algorithms that are designed to automatically adapt to the circumstances. Additionally, software algorithms can be up-

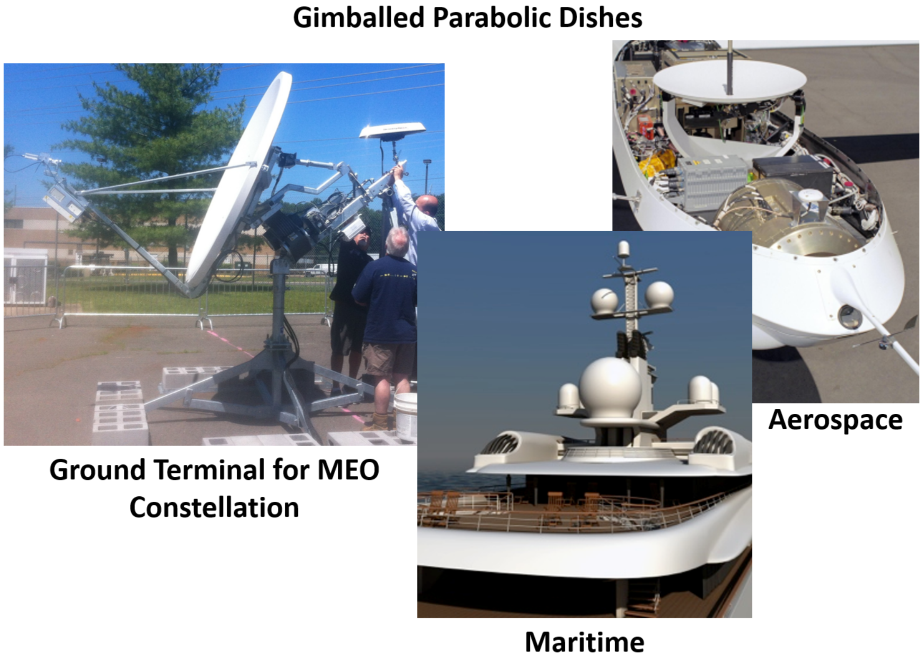

Figure 1.2: Gimballed parabolic reflector antennas in mobile applications. Gimballed reflectors are heavy, bulky, and require significant human intervention for setup and maintenance due to the mechanically moving parts.

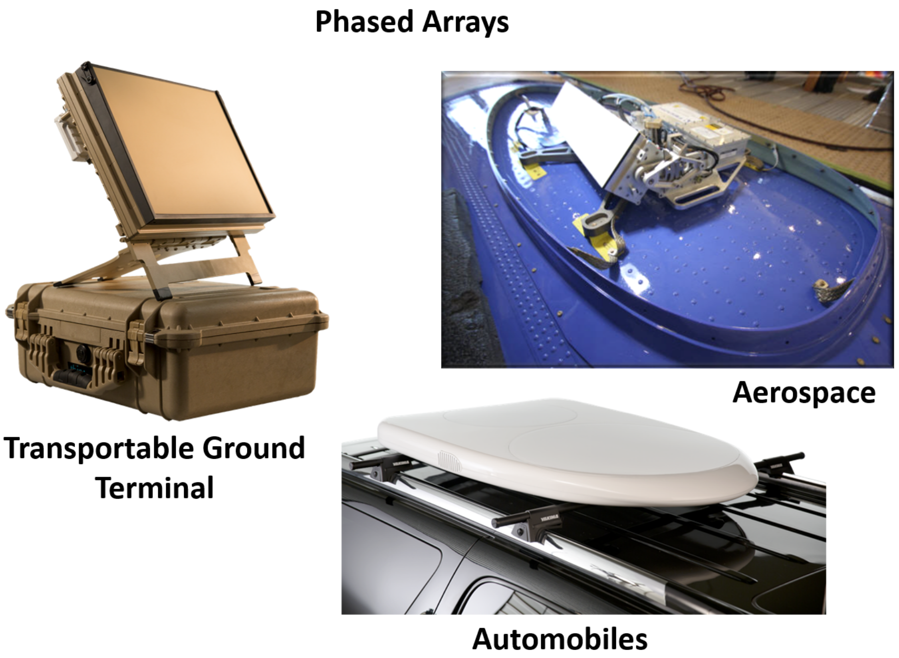

Figure 1.3: Phased array antennas in mobile applications. Phased array antennas consume large amounts of power to operate, require additional cooling, and are expensive to manufacture. Also, today's phased array systems for commercial mobile applications often still rely on some mechanical steering to achieve the full scanning requirements of mobile consumers.

graded remotely to introduce new functionality that can enable new applications and improved performance without change of architecture. For example, the software control of the antenna ensures that the main beam points in exactly the desired direction, that it achieves as much gain as is allowed by the hardware designs, that unwanted radiation does not occur to degrade the signal-to-noise ratio or interfere with other transmissions, and that specific interference from other transmissions is mitigated with null steering. Also, smart software can mitigate variations in individual antennas; adaptive algorithms allow each antenna to learn its own optimal controls. Finally, the flexibility of adaptive, real-time software engineering also allows the antenna to handle changing conditions - environmental and internal

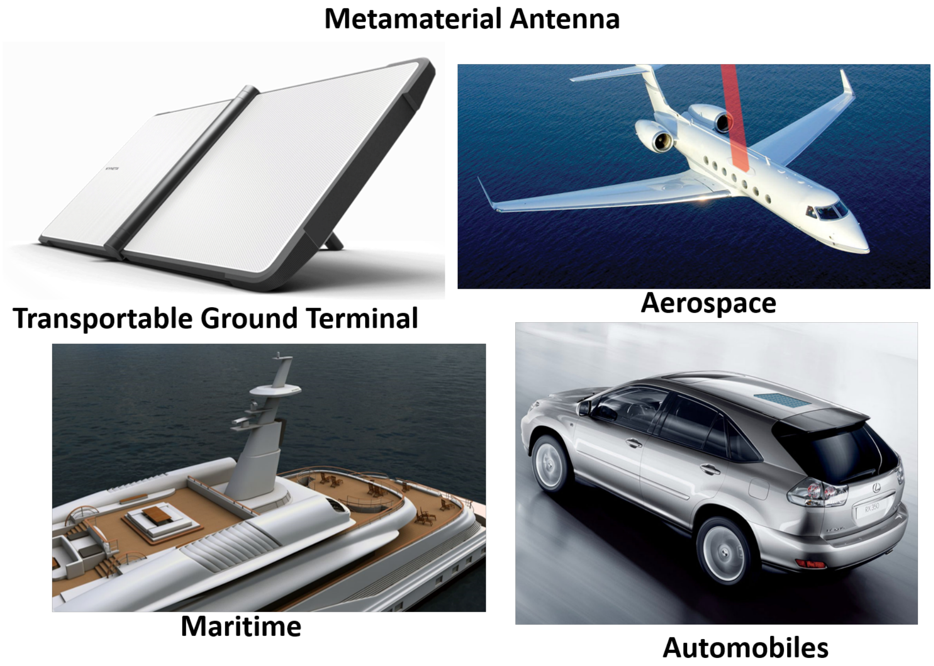

Figure 1.4: The metamaterial antenna in mobile applications. The metamaterial antenna is thin, light-weight, consumes little power, and does not have expensive components like the phased array. The metamaterial antenna is capable of electronic beam steering, which is an advantage in mobile applications, reducing setup and maintenance.

- that occur during prolonged operation in the hands of users.

The importance of live, on board, software-controlled, machine-intelligent optimization of the antenna cannot be understated. Even if the hardware designs were perfect and manufactured perfectly, without reliable, robust, optimal software control ensuring continuous high performance, the metamaterial antenna would be little better than a fixed parabolic reflector antenna. Just as advanced software has improved medical imaging making diagnoses more accurate and less invasive and as advanced feedback-control is frequently used to upgrade U.S. fighter plane capabilities without hardware modification, so, too, is smart software for the metamaterial antenna both necessary and ripe for the advancement of the technology.

To date, development has largely been in physical designs of the metamaterial antenna (see [14] and the references therein). On software-control aspects, these works have pointed

Table 1.2: Performance characteristics of antennas for mobile satellite communications

Parameter	Gimballed Reflector	Phased Array	Metamaterial
Beamsteering	Mechanical	Electronic	Electronic
Weight (Kg)	130	150-250	20
Height/Diameter (cm)	150/130	5-30/100	3-5/100
Power Req.-Beamsteering (W)	>200	>1,000	3
Size Req.-100 Mbps Rx/10 Mbps Tx	Not capable	<1 m square	<1 m diameter
Maintenance Req.	High	Low	Low
Cost	Low	High	Low

to phased array and holographic antenna literature to give basic theory and highlight the possibilities that *should* exist based on the metamaterial antenna's phased array-like characteristics. Yet, little on the control side has been demonstrated (partially because the hardware development to reach the point of being able to study and test software control has been so consuming).

This thesis represents a significant advance in the area of smart metamaterial antenna control. It approaches a complete mathematical framework for an adaptive, self-optimizing metamaterial antenna, endowing the metamaterial antenna technology with machine intelligence for intervention-free, dynamic operation.

1.2 A Reconfigurable Holographic Metamaterial Antenna (RHMA)

The type of metamaterial antenna considered throughout this thesis is called a *Reconfigurable Holographic Metamaterial Antenna* and will be frequently referred to as an RHMA. In this section, a detailed description of the RHMA is given. It is helpful when discussing this technology to build the description of the RHMA from its constituent parts, starting with the term "antenna."

Everyone is familiar with what an antenna does whether or not they are familiar with how

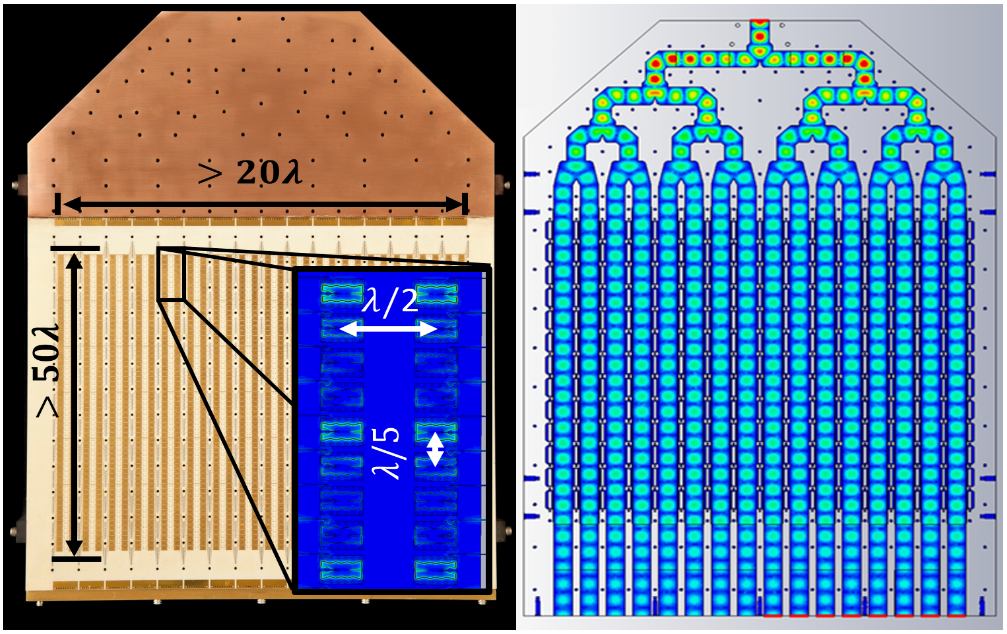

Figure 1.5: (Left) Top-view of a holographic metamaterial antenna, which is composed of a planar array of metamaterial unit cells (seen in the inset) fed by parallel rectangular waveguides beneath the unit cells. (Right) The parallel rectangular waveguide feed structure of the holographic metamaterial antenna. Parallel waveguides propagating the primary TE_{10} mode feed columns of metamaterial unit cells.

an antenna works. An antenna is a reciprocal device that converts electric power into electromagnetic waves. An antenna is the device by which a guided wave (typically containing encoded information) is transferred to free space where it propagates, without active interference, and is sensed/received at some other location (reversing the process to recover the transmitted information). Antennas are an old field of study typically credited to Faraday in the 1830's. Then, Hertz demonstrated wireless communication with the dipole antenna in 1886, and by 1901 Marconi was sending and receiving wirelessly across the Atlantic ocean with vertical wires [15]. Today, antennas are ubiquitous, operating in a wide range of frequency bands, in the home and office, on cars, planes, trains, boats, cell phones, etc.

Onto "antenna" is layered "metamaterial." The metamaterial of this work consists of a planar array of densely-packed resonant unit cells. See the left pane of figure 1.5 for a picture of the planar metamaterial and the inset of figure 1.5 for a picture of several unit cells. The cells are arrayed on the surface such that there are rows of cells that are near together at a spacing of approximately $\lambda/5$ (where λ is the wavelength at the frequency of operation of the antenna, e.g. 1 cm at 30 GHz or 1.5cm at 20 GHz), and the separate rows are arrayed at a greater spacing of approximately $\lambda/2$, again refer to the inset of figure 1.5. It is this plane of metamaterial that is the interface between the guided wave of the antenna and free space. It is this interface, and the control of this interface, that permits the RHMA to specify in which directions the radiation of the antenna occurs. On the guided-wave side of the metamaterial interface is an array of parallel rectangular waveguides such that each row of unit cells is above each waveguide channel. In this way, an entire row is fed by a single waveguide, see the right image of figure 1.5. This array of waveguides confines and propagates the radio frequency wave containing encoded data, and as it propagates past the metamaterial unit cells, the metamaterial allows carefully controlled radiation of this wave to free space.

The next term is “holographic.” Holography will be explained mathematically in detail in chapter 3, so here I simply say that the principle of holography is how one selects where the energy of the waveguides is radiated by the metamaterial. Briefly, as in Princess Leia’s plea to Obi Wan Kenobi, holography is a means of recording and then “playing back” a three-dimensional image. In the case of the metamaterial antenna, the desired image is the one pin-prick in space that one wants all the energy of the antenna to radiate toward (the satellite). The metamaterial antenna is the surface upon which the image is recorded, and it is “played back” by the guided waves underneath.

Finally, we arrive at “reconfigurable.” The idea of reconfigurability of the metamaterial antenna is that it is possible, in real-time, to change the recorded holographic image, and so, change the radiation direction of the antenna’s energy. The metamaterial unit cells are the means by which the holographic image is recorded, so reconfigurability of the holographic metamaterial antenna ultimately means changing the radiation characteristics of the individual metamaterial unit cells to change the holographic image.

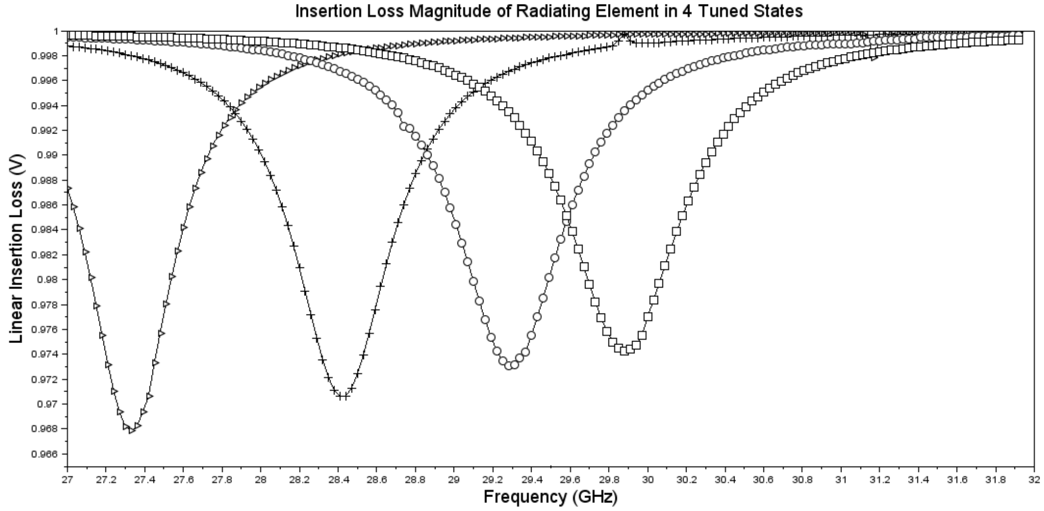

Figure 1.6: Example of four voltage-tuned metamaterial unit cell states. The tuning of the unit cell shifts the resonant frequency of the cell nearer to or further from the antenna's operating frequency. When the resonance of the cell is close to the operating frequency, the cell radiates a maximum amount of energy. Conversely, when the resonance is far from the operating frequency, the cell radiates a minimum amount of energy.

For the antenna studied in this thesis, the resonant frequency of each unit cell is changed by the application of a voltage to each. This tuning shifts the resonance of the cell nearer to or further from the operating frequency of the antenna. Figure 1.6 shows the cell response for four different voltage-tuned states for an example unit cell. In this example data, when the cell has no voltage applied to it, the cell resonates at 29.9 GHz, but when the cell is fully biased, it resonates at 27.3 GHz. The two intermediate voltage levels cause the cell to resonate in between the uppermost and lowermost possible resonances; in this way, the voltage-control of the antenna can continuously vary the cell response to achieve any state between the two extremes.

When tuned to a resonance far from the operating frequency, the cell scatters little energy into free-space. This state is called "off" or, when parameterized, 0. On the other hand, when tuned such that the resonance is close to the operating frequency, the cell scatters a maximal amount of energy. Thus, this state is called "on" or, parametrically, 1. Then, as mentioned before, holography indicates how on or off each cell should be to record the desired image, pointing the beam in the desired direction.

Taken all together, the reconfigurable holographic metamaterial antenna is described with its means of controlling the radiation of the antenna and its means of real-time reconfigurability. It is this antenna whose adaptive control is studied in this thesis. An example antenna for the application of high-throughput satellite communications may be of the approximate dimensions shown in figure 1.5 of $20\lambda \times 50\lambda$ and less than half an inch thick. An antenna this size has more than ten thousand independently controlled cells. The problem of designing intelligent, self-optimizing algorithms for the RHMA is specifying the best controls across so many cells for all scan angles, in all environments, for each individual antenna, quickly enough for mobile applications.

In subsequent chapters, I will again briefly describe the characteristics of the RHMA. In each chapter, I describe the RHMA's peculiarities as they relate to the problem solved in that chapter. In chapter 2, I describe the characteristics of the antenna that are of direct consideration in the modeling process of the antenna, and in chapter 3, I describe the characteristics of the antenna that pose particular problems for pattern synthesis.

1.3 Thesis Outline

In this thesis, I take three major steps toward an adaptive, self-optimizing reconfigurable holographic metamaterial antenna. First, I develop a computational model of the antenna to predict its behavior. Second, with a fast and accurate model in hand that allows me to study and understand the major problems in the RHMA far-field pattern, I derive a pattern synthesis technique to suppress the sidelobes indicated by the computational model. Finally, I design and demonstrate an adaptive control approach that builds onto the pattern synthesis method to continuously, during operation by any user, allow the antenna to improve its beam performance.

Thus, the progression of this thesis is as follows. In chapter 2, I develop the metamaterial modeling technique that I adapted specifically for the prediction of the behavior of the metamaterial antenna. This modeling technique is derived from the discrete-dipole approximation, and it captures more of the complex, coupled physics of the metamaterial antenna than other standard analytic techniques. It is also much faster than full-wave simulation, the benchmark for accurate numerical electromagnetic simulations. I show results demonstrating that this modeling technique is more accurate and better able to predict the beam pattern of the metamaterial antenna than other methods. This predictive modeling enables me to begin work in finding pattern synthesis techniques to optimize the antenna's beam performance.

In chapter 3, I design a new approach to pattern synthesis for the RHMA that is able to suppress targeted sidelobes. In this chapter, I first explain pattern synthesis for the RHMA from a familiar phased array perspective, and then further explain the same pattern synthesis procedure based on the principles of holography. Each approach gives a useful perspective on pattern synthesis for the RHMA, and helps to identify various causes of sidelobes, indicating directions for improved control of the antenna. Next, I introduce the theory of sidelobe cancellation on a holographic antenna and develop an optimization scheme to identify the pattern parameters providing optimal sidelobe. The efficacy of this pattern synthesis optimization theory is then demonstrated both in simulation and on a hardware device.

While the pattern synthesis technique of chapter 3 is successful in reducing unwanted sidelobes, it remains a step short of an *adaptive antenna* because the optimization approach is not suitable for continuous optimization during operation. In addition, the objective function pursued in the optimization is narrow in its applicability, and it cannot be measured in real-time. In chapter 4, I introduce an *extremum-seeking controller* that is capable of synthesizing reduced-sidelobe control patterns using the technique of chapter 3 in a viable and robust manner for live, on board optimization. In this chapter, I also investigate the objective function used with the extremum-seeking controller. Then, to further improve the viability of the adaptive control approach, I combine the controller with value function approximation to dramatically reduce the time-to-optimization.

Finally, I conclude this thesis with a summary and outlook, chapter 5.

Chapter 2

DISCRETE-DIPOLE MODELING OF A RHMA

2.1 Introduction

Metamaterials are not a new field in theory; engineered materials with simultaneous negative permittivity and permeability were hypothesized by Veselago as early as 1968 [16]. However, it was not until 2000 that the first metamaterial was experimentally demonstrated by Smith et al. [17]. Because they have fundamentally changed what is believed possible to realize in terms of exotic material characteristics and the extraordinary impact this could have on any number of engineering applications, their study has attracted considerable interest and has seen explosive advance in the last 15 years [18, 19, 20, 21]. Much work has been focused on theoretically developing and describing metamaterials to efficiently and accurately design them to achieve the desired material characteristics (e.g. transformation optics [22, 23]).

Many metamaterial modeling methods have been posited and studied to capture properties of the material response that are of interest in various applications including electromagnetic scattering, energy losses, and continuum properties. As one would expect, metamaterial modeling has taken a variety of classical modeling techniques and attempted to adapt them to the peculiarities of the metamaterial - the uncommon length scales and configurations. These methods include homogenization [24, 25], Lagrangians [26, 27, 28], multipole methods [29, 30], discrete-dipole approximation (DDA) models [31, 32], and circuit equivalents [33]. However, until now, these models have not been studied for the purpose of accurate prediction of the far-field pattern of a dynamically tunable metamaterial antenna.

In this chapter, I adapt and study a discrete-dipole approximation (DDA) model of a planar metamaterial to predict the far-field radiation when the metamaterial is excited by a guided wave. I demonstrate that some other common models, a circuit equivalent (as in [33]) or a simple array factor model (as in [3]), are insufficient for high-fidelity prediction of the far-field radiation. An accurate model is imperative to be able to design pattern synthesis approaches that improve the performance of the antenna. An inaccurate model will lead to two problems. First, without accurate prediction of the radiation pattern, one may end up identifying a problem that does not exist while missing a real problem. Second, an inaccurate model of the antenna response will likely lead to an incorrect solution on top of having potentially identified the wrong problem.

In the next section, I describe the challenges and goals for a computational model of the metamaterial antenna and introduce the discrete-dipole approximation. I then derive the DDA model for the metamaterial antenna. In section 2.3, I demonstrate the accuracy of the DDA model in predicting the far-field pattern of the RHMA as compared with other methods, benchmarking against full-wave simulation.

2.2 Analytic Derivation of the Discrete-Dipole Model of a RHMA

In this section, I develop the discrete-dipole approximation model for the RHMA. I discuss the properties of the metamaterial antenna that make fast, accurate prediction of its far-field difficult, and I also address the required characteristics of the computational model. Next, I introduce the DDA generally before deriving the DDA model specific to the RHMA.

2.2.1 Metamaterial modeling

Metamaterials, being comprised of macroscopic unit cells with characteristic dimension on the order of an operating wavelength (λ), pose an interesting modeling problem. Unit cell geometries include split-ring resonators (SRRs), double SRRs, complementary SRRs, cut-wire pairs, continuous wires, fishnet structures, and chiral elements - all typically of dimension between $\lambda/2$ to $\lambda/20$. The length and frequency scales on which a metamaterial can be considered a continuum material are much larger and much lower, respectively, than traditional materials comprised of microscopic molecules. This structural scaling results in a blurring of the boundaries between the applicability of macroscopic and microscopic electromagnetic modeling techniques (see [25] and the references therein and [34, 35] for excellent discussions on the often-ignored assumptions on size and configuration of the unit cells that can make the modeling of metamaterials with homogenization and other averaging techniques rapidly degrade in accuracy). Thus, the first problem of metamaterial modeling with most classical material techniques is that the metamaterial dimensions run very near to the modeling break-down point.

Further, the metamaterial antenna considered in this work differs from the generic metamaterial in several important ways that are important to the design of the mathematical model. For one, the typical metamaterial, like the first metamaterial demonstrated for electromagnetic cloaking, are regular three dimensional lattices of unit cells [36]. On the other hand, the metamaterial antenna I consider is a regular 2D lattice with unequal spacings. Thus, volumetric averaging is not possible for the metamaterial antenna as it is for the 3D metamaterials. As such, the chosen modeling method must accurately model both the unequal lattice spacing and the fact that every single element is a boundary element (in the third dimension).

Additionally, the metamaterial antenna produces a holographic pattern on the array to steer the radiated energy in the desired direction. To accomplish the recording of all of the holographic patterns that produce beams at varying scan angles, each element must be individually driven to obtain different cell properties. That is, unlike metamaterials where each constituent cell is uniform, each cell in the antenna array is tuned to a unique state at any given time. In this way, it is imperative that the chosen model is able to innately capture the resulting collective response from the individual cells, each at a different response state.

Another difference from the typically considered metamaterial is the form of the applied electromagnetic field. Commonly, the applied electromagnetic field is a plane or spherical wave propagating in free-space. In the case of the metamaterial antenna, the wave incident on the metamaterial is the field confined to the rectangular waveguide. This confinement induces reflections and other interactions inside the cavity that cannot be discounted in the aim to produce an accurate prediction of the collective behavior of the antenna.

Finally, the antenna is composed of tens of thousands of individually tuned unit cells to produce a high-gain beam. Yet, the forward dynamic model must be able to quickly produce an accurate far-field pattern for any combination of these thousands of unit cell controls to enable model-based control in a real-time application or simply to do many simulations of possible approaches for the purpose of experimentation with pattern synthesis. The most accurate numerical modeling technique, full-wave simulation, is prohibitively time-intensive even for modestly sized arrays of just a couple hundred cells when considering the requirements of iterative experimentation. It is my primary goal in developing this DDA model of the antenna to achieve a fast and accurate modeling tool that enables the pursuit of pattern optimization and adaptive control of the entire RHMA.

I have identified several difficulties in metamaterial antenna modeling: the scale of the unit cell structures, the two-dimensional lattice structure, the integral property that the cells all be permitted unique response characteristics, the form of the applied field, and the sheer number of cells to be modeled. One or more of these challenges poses a particular problem to each of the common techniques [24, 25, 26, 27, 28, 29, 30, 33]. For example homogenization is not well-suited to the 2D structure of the metamaterial - the averaging process is suspect when all cells are boundary cells. And, the Lagrangian is not innately capable of handling the guided-wave excitation. And, finally, as noted before, the accuracy of full-wave simulation is simply too computationally intensive for the pattern synthesis aims. On the other hand, the discrete dipole approximation is able to mathematically consistently handle the 2D arrangement of unit cells, the guided wave excitation, the individual tuning of the elements, and the DDA solution is fast to compute.

2.2.2 Discrete-dipole approximation

The discrete-dipole approximation is a method for computing the scattering of electromagnetic energy by an arbitrarily shaped object. First introduced by DeVoe [37] in 1964 to study solid collections of molecules, the DDA has matured to a general numerical technique for computing electromagnetic scattering (see, e.g., [38, 39, 40]).

There are two useful interpretations of the derivation of the DDA. First, the DDA may be viewed beginning from the integral form of Maxwell's equations for time-harmonic electromagnetic fields. Then, to make the solution of the integral equations computationally tractable, the DDA discretizes the volume of the scatterer into subvolumes, each of which is characterized by a single polarization (dipole response) (see Yurkin's review in 2007 in which he unified all the DDA variants at the time [39]). On the other hand, the DDA can be viewed as it was originally derived by DeVoe. He was inspired by Lorentz's discovery that the dielectric properties of a substance can be directly related to the polarizabilities of the individual atoms of which it is composed. With this interpretation, DeVoe reasoned that one could discretize a large solid scatterer by a collection of point dipoles contained in the bounding geometry of the scatterer. Based on Lorentz's discover, in the limit as the number of discrete dipoles approached infinity, every molecule of the scatterer is replaced and accurately modeled with dipolar reponse. The DDA then uses the linearity of Maxwell's microscopic equations to derive Maxwell's macroscopic equations as a summation of the behavior of the point dipoles (as opposed to the previous interpretation of arriving at a summation by discretization of the integral form of Maxwell's equations). Importantly, Flatau points out that, "For a finite array of point dipoles the scattering problem may be solved exactly, so the only approximation that is present in the DDA is the replacement of the continuum target by an array of N-point dipoles [38]." Interestingly, in this way, the DDA solves the first problem of metamaterial modeling - the problem of the scale of the constituent material components. The DDA is a consistent formulation of Maxwell's equations spanning multiple scales.

In a metamaterial, each unit cell, be it SRR, double SRR, or cut-wire pair, responds to a locally applied electromagnetic field. It is, thus, reasonable to represent each cell's response to the local field as a single electric dipole response (higher order multipoles may also be consistently incorporated into the model, if desired). In total, the DDA replaces the large solid scatterer of the full metamaterial by a collection of point-dipoles contained in the geometry of the scatter that are, not coincidentally, collocated with the metamaterial unit cells. In this way, the DDA is a logically accurate way to approximate Maxwell's equations to tractably solve for the electromagnetic scattering of a metamaterial.

2.2.3 DDA for a RHMA

The DDA model for a 2D metamaterial is derived by replacing each of the N complex unit cell resonators (each of which is individually tuned) at locations $\mathbf{x}_i, \forall i = [1, 2, ..., N]$ with a point-dipole at the same location.

Before deriving the mathematical formulation of the DDA model, I first give some notation. I will use indices i and j to denote cell locations and the notation $\forall i$ and j implies $\forall i, j \in [1, 2, ..., N]$.

I will denote the total field experienced at any position in the waveguide $\mathbf{x}$ as $\mathbf{E}^{tot}(\mathbf{x})$. This total electric field can be expanded into any chosen basis, but as the antenna system is excited by a traveling electromagnetic guided wave, it is natural to expand the electric fields in terms of waveguide modes into $m = 1, 2, ..., M$ waveguide mode components such that, $\mathbf{E}^{tot}(\mathbf{x}) = \Sigma_{m=1}^{M} \mathbf{E}_m^{tot}(\mathbf{x})$; similarly to the cell locations, I reserve the notation $\forall m$ or n to mean $\forall m, n \in [1, 2, ..., M]$. The dominant excitation of the metamaterial will be from the propagating mode; however, as I am also considering interactions among dipoles having spacing much less than a wavelength, I cannot discount the excitation of and interaction with higher order waveguide modes by the unit cells themselves.

Finally, define the m-th mode scattered field of any resonator i experienced at any position in the waveguide $\mathbf{x}$ as $\mathbf{E}_{i,m}^{scatt}(\mathbf{x})$. One subtlety of this definition is the fact that $\mathbf{E}_{i,m}^{scatt}$ is undefined when evaluated at the location of cell i. That is, the scattered field of cell i is not "felt" by cell i. Then, the exciting (equivalently, incident field) of any single dipole is the total field minus any fields that are generated by that dipole.

With these field definitions, the linearity of Maxwell's equations permit one to describe the total field in the waveguide as a linear combination of the scattered fields of the dipole-modeled resonators plus an external field, $\mathbf{E}_m^0$:

$$\mathbf{E}_m^{tot}(\mathbf{x}) = \mathbf{E}_m^0(\mathbf{x}) + \Sigma_{i=1}^{N} \mathbf{E}_{i,m}^{scatt}(\mathbf{x}), \forall m. \tag{2.1}$$

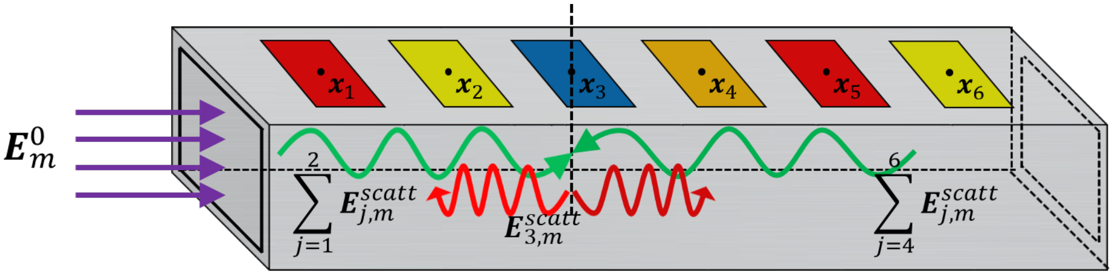

Figure 2.1: Illustration of the induced scattering of cell 3 (dotted arrows) due to the applied field $\mathbf{E}^0$ and the summary effect of the scattered field of all the other cells (solid arrows).

I once more highlight that if $\mathbf{E}^{tot}$ is evaluated at a location $\mathbf{x}$ which is coincident with a resonator, say $\mathbf{x}_j$, the summation over the scattered fields will omit the index $i = j$, and may be referred to as the incident field on resonator j. Figure 2.1 illustrates equation 2.1 for a small number of cells. In particular figure 2.1 illustrates the fields experienced by cell 3 and the resulting scattering response of that same cell. Additionally, note that working from the Maxwell's equations, one already has a means inherent to the model to handle the guided wave excitation $\mathbf{E}_m^0$.

Each dipole has a polarization that is proportional to the incident field:

$$\mathbf{P}_{j,m} = \bar{\bar{\alpha}}_{j,m}\mathbf{E}_{j,m}^{tot}(\mathbf{x}_j), \forall j \text{ and } \forall m, \tag{2.2}$$

where $\bar{\bar{\alpha}}_{j,m}$ is the complex polarizability tensor of cell j in the m-th mode. By choice of the coordinate system orthogonal to the principle response directions of the dipole, one can take the polarizability tensor to be diagonal. Then, to simplify further, one may assume isotropy such that the polarizability tensor becomes a scalar multiple of the identity tensor, effectively reducing the tensor $\bar{\bar{\alpha}}_{j,m}$ to a scalar α_j for each cell.

One further subtlety in concept and notation regarding field quantities in the DDA is the relationship between the incident field and the scattered field at the location of the dipoles. I noted earlier that the concept of the scattered field is poorly defined at the location of the cell. Rather, it is the idea of the induced field elsewhere in the waveguide due to an incident field on a particular dipole. It is helpful to explicitly define the relationship between the incident field on a cell and the scattered field of the same cell. This relationship is referred to as “coupling” and is quantified by the “coupling coefficient” which is given by [31]:

$$\mathbf{E}_{j,m}^{scatt} = \sum_{n=1}^{M} \mathbf{C}_{j}^{m,n} \mathbf{E}_{n}^{tot}(\mathbf{x}_j), \forall j \text{ and } \forall m. \tag{2.3}$$

One may further divide the coupling behavior by substituting the summation expression for the total incident field of equation 2.1 into equation 2.3:

$$\mathbf{E}_{i,m}^{scatt} = \sum_{n=1}^{M} C_{i,0}^{m,n} \mathbf{E}_{n}^{0} + \sum_{n=1}^{M} \sum_{\substack{j=1 \\ j \neq i}}^{N} C_{i,j}^{m,n} \mathbf{E}_{j,n}^{scatt}. \tag{2.4}$$

where the notation $C_{i,j}^{m,n}$ is interpreted as the amount of energy that is scattered by the m-th mode of cell i due to coupling to the scattered n-th mode of cell j. The coupling coefficients, may be directly extracted from full-wave simulation as is indicated in the following section 2.2.3.

Equation 2.4 is a self-consistent matrix system of equations of dimension $NM \times NM$ to solve for the scattered field of each resonator. One solves this equation for the scattered fields of each resonator and then use equations 2.1 and 2.2 to obtain the total field in the waveguide and retrieve the polarization of the unit cells.

After solving for the polarization, one can compute the far-field radiation characteristics of the array of dipoles using traditional array factor analysis [41]:

$$AF(\theta_0, \phi_0) = \sum_{j=1}^{N} \mathbf{P}_j \exp(-i\mathbf{k}_f(\theta_0, \phi_0) \cdot \mathbf{r}_j), \tag{2.5}$$

where $\mathbf{k}_f(\theta_0, \phi_0)$ is the desired directional complex propagation vector in free space, and $\mathbf{r}_j$ is a coordinate of cell j radiator on the surface of the antenna (which may or may not be identical to the coordinate in the waveguide $\mathbf{x}_j$ depending on the choice of coordinates for the two different calculations). I next discuss how to obtain the coupling coefficients and the polarizability which are requisite to accurately capture the interaction of a cell with an incident field.

Extraction of coupling coefficients

To define the coupling coefficients between cells for the M waveguide modes, one does a full-wave simulation of a single unit cell (though measurement could also be used) to empirically define the relationship between the electric field at points one can measure (waveguide ports) and the electric field at the scatterers.

While the framework of coupling coefficients in equation 2.4 is completely general, in defining coupling coefficients specifically for the traveling-wave fed array, notice that a cell upstream of a cell of interest has a much greater effect than a downstream cell because an upstream cell effects the strong, forward propagating wave before it reaches the cell of interest whereas a downstream cell only affects an upstream cell through a weak backward propagating scattered or reflected wave. So, one defines coupling values for the two cases: $i < j$ and, separately, $i > j$.

The derivation of the coupling coefficients is consigned to Appendix A.1, but I state here that they are:

$$C_{i,j}^{m,n} = S_{21}^{m,n} - \delta_{ij}, \forall i > j \quad [j \text{ upstream of } i], \tag{2.6}$$

$$C_{i,j}^{m,n} = S_{11}^{m,n}, \forall i < j \quad [j \text{ downstream of } i], \tag{2.7}$$

From full-wave simulation of a single resonant cell, one obtains the scattering parameters for the multiple achievable states of a tunable unit cell (recall figure 1.6). Thus, one constructs the relevant entries of the matrix system of equation (2.4) for each cell using the coupling coefficients defined by the appropriate scattering parameter curves. In this way, the DDA model is flexible in handling cells with different behavior on a per-cell basis.

Definition of polarizability

The definition of the polarizability, $\alpha_{j,m}$, of each cell is the primary gradation among DDA variants [39]. In the initial works, the polarizability was defined based on the Clausius-

Mossotti relation stating:

$$\alpha_j = \frac{3d^3}{4\pi}\frac{\epsilon_j - 1}{\epsilon_j + 2}, \tag{2.8}$$

where ϵ_j is the continuum dielectric constant of the j-th dipole and d is the distance between cells. This relation is exact in the case of a repeated, infinite cubic lattice. Many modifications of this definition have been proposed to handle non-cubic lattices and, importantly, to retain conservation of energy, see [39] for a review.

Recall that the polarizability relates the total incident field on a dipole to the resulting polarization of the dipole. Thus, the amplitude of the polarization is the difference between the input power and the out-going power in the waveguide which is measured as return loss S_{11} and insertion loss S_{21} and which must be scaled by the radiation efficiency of the cell, ϵ_{rad}. In essence, energy not remaining in the waveguide and not lost to inefficiencies is radiated, is the resulting magnitude of polarization of a cell.

Also, the phase component of the polarizability indicates the amount by which the resonator shifts the phase of the incident field. Again using full-wave simulation, one empirically finds that the scattered phase is nearly equivalent to the angle of the return loss measurement. Note that this is not surprising. If one models the cell as a serial shunt impedance in an equivalent circuit, the phase of the insertion loss is directly proportional to that of shunt impedance which gives the Lorentzian dispersion as was used by Lipworth [3].

Combining the amplitude and phase considerations of the previous two paragraphs, one may completely define the polarizability of a cell as:

$$\alpha = \epsilon_{\text{rad}}\sqrt{1 - |S_{11}|^2 - |S_{21}|^2}\angle S_{11}. \tag{2.9}$$

Here, again, the polarizability of each unit cell is defined individually for each cell allowing each cell to be take on independent values based on its individual control state, which is of paramount importance for accurate prediction of the antenna's far-field.

2.3 Numerical Results Using the DDA Model of a RHMA

In this section I give numerical examples of the use of the DDA model for two parallel rows of metamaterial unit cells each row comprising two hundred dynamically configurable metamaterial elements fed from the same end of the waveguide. The cells are spaced at $\lambda/5$ down the waveguide and at $3\lambda/5$ between the two rows.

The far-field result of two different control patterns for the four hundred individual cells (the same tuning control was applied to each of the two rows; effectively 200 independent controls) are shown on the left of figures 2.2 and 2.3. In each plot the normalized directivity of the computed patterns under an ideal array factor, the circuit equivalent model, and the DDA model are compared against full-wave modeling in CST Microwave Studio Suite$^{\mathrm{TM}}$. (Both the ideal array factor model and the circuit equivalent model particular to the geometry of the antenna considered in this work are given in appendix A.2.) The relative L_2 error of each model in the range ± 5 degrees θ is given in the inset and indicates that the DDA model is better than 2.5 times more accurate than the second best model, the circuit equivalent, in these two example patterns.

In addition, a close-up view of the main beam for each of the patterns is shown on the right of figures 2.2 and 2.3. These views show the ability of the DDA model to correctly predict the main beam width for both patterns.

It is significant to my purpose in the rest of this thesis, developing adaptive control of the RHMA, to note that both patterns demonstrated here create a main beam at broadside, but the sidelobe pattern is dramatically different between the two. This one simple result has significant implications for control and optimization of the radiation pattern, generally. Even with only two hundred independent variables to control, one can design many different patterns that still result in a beam pointing in the same direction (many more than just the two demonstrated here). Therefore, there is redundancy in the control space. This redundancy is required to be able to electronically scan the beam to wide-angles and achieve pointing accuracy, and this high-degree of redundancy points to much room for optimization

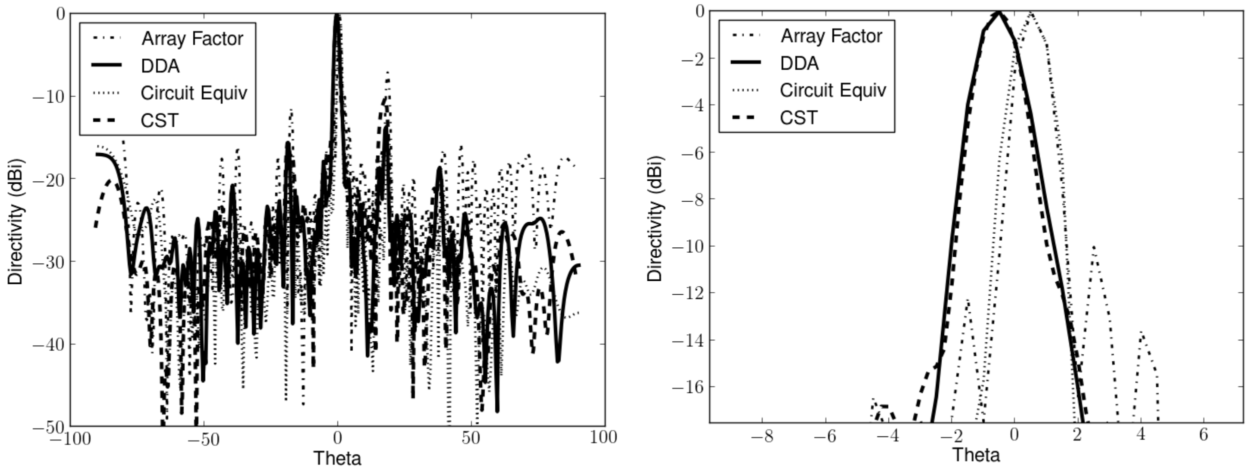

Figure 2.2: Far-field radiation pattern of a 2 × 200 array of resonators at broadside. (Left) 1D far-field pattern slice $\theta = [-90, 90]$ taken parallel to the channels. (Right) Close-up view of the main beam, which shows the DDA model's excellent matching of the main beam to the CST full-wave result. The full-wave solution generated by CST (dashed) is considered the most accurate achievable numerical solution to which all models, particularly the DDA model developed in this work (solid), should be compared.

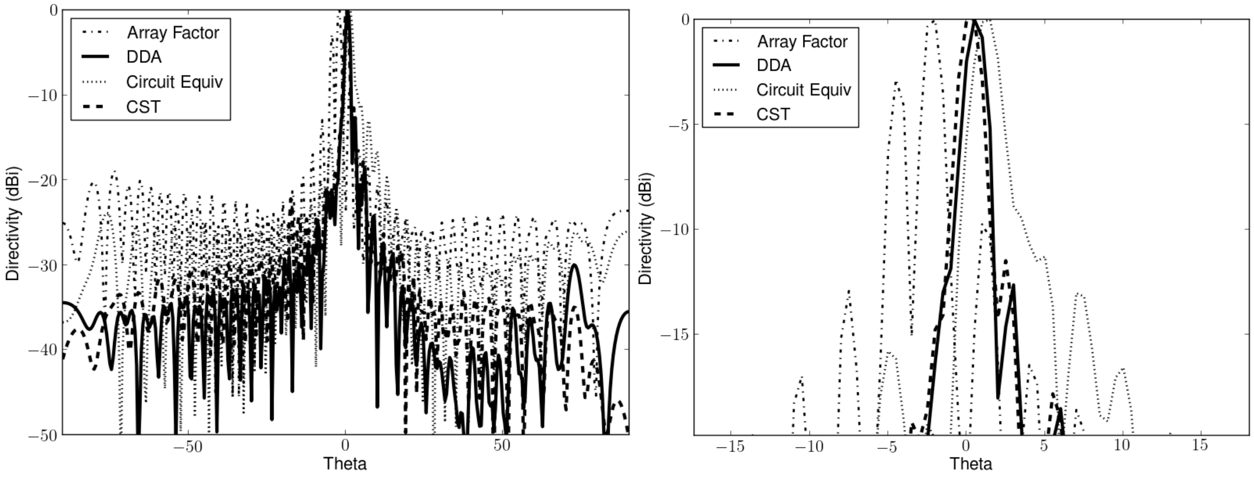

Figure 2.3: A second, improved far-field radiation pattern of a 2 × 200 array of resonators at broadside. (Left) 1D far-field pattern slice $\theta = [-90, 90]$ taken parallel to the channels. (Right) Close-up view of the main beam, again demonstrating the DDA's accuracy in predicting the far-field pattern of the metamaterial antenna.

to obtain desired characteristics of a far-field pattern. In the next chapter, I identify the low-dimensional parameter space that causes a main beam to point in the desired direction, and then I add to this low-dimensional space, consuming more of the antenna's control degrees of freedom, to constrain the antenna, providing an improved radiation pattern.

The aim is to achieve optimal performance over all scan angles, over all environmental conditions experienced by the antenna, and over all the variances between individual antennas, by studying and optimizing the pattern synthesis on the modeled antenna. However, one would be seriously misled if one were to optimize the beam by evaluation of the criteria of sidelobe level with the array factor model or the circuit equivalent model; the pattern predicted by the ideal array factor model of figure 2.3 indicates a split main beam which does not appear in the full-wave result. To be assured that the pattern synthesis experimentation is, in fact, effectively targeting the real beam-performance issues experienced by the RHMA design, one must use a most accurate computational modeling tool. I have demonstrated here that the DDA model is the best of the investigated tools, apart from full-wave simulation, for accurate predictive modeling of the far-field of the metamaterial antenna.

2.3.1 Computational time

Modeling of a metamaterial array in full-wave simulation (apart from the geometric model-building and post-processing to obtain the far-field pattern and other derived quantities) has 2 steps, both of which are computationally intensive for a full-sized antenna: accurately applying a mesh the 3D geometry and solving the discretized Maxwell's equations on this mesh. As a small example, the modeling of this 2×200 cell strip in the frequency domain in CST Microwave Studio took 9 adaptive meshing passes requiring 2.5 hours on a desktop machine with Intel Xeon(R) processors with 192GB of RAM. Then the solution of Maxwell's equations on this mesh took approximately 35 minutes per frequency point. Also, the entire simulation process, all 3 hours of it, must be undertaken any time the characteristics of any individual unit cell are modified. Finally, the computation time grows exponentially with the size of the metamaterial array being simulated, quickly becoming prohibitively long. It is certainly infeasible to model a full antenna of 10,000 cells thousands of times to study pattern synthesis.

On the other hand, modeling of the single unit cell required for the parameter extraction of the circuit model or the DDA model required only 20 minutes per cell state (meshing, solving, and post-processing). It is necessary to model at least two states, the maximal and minimal resonant frequency states, bringing the minimum time for parameter extraction for the DDA model via simulation to 40 minutes. However, this simulation can be done once for any unit cell design. Then the analytic model, DDA or circuit equivalent, can be used to model any geometric configuration of the cells as well as any control pattern.

The DDA model does require inversion of a dense $NM \times NM$ matrix, but, since the matrix dimension grows only linearly with the number of cells, we are able to easily model an array of even 20,000 cells on a common desktop computer in seconds. The circuit equivalent model does not require inversion of a large array, but the cascading matrix approach requires looping twice through all the elements performing small (2×2) matrix-vector multiplications. The resulting computation time of the DDA and the circuit equivalent are similar, yet the DDA provides more accurate predictive results.

Summary

In this chapter, I have derived a DDA model for the planar reconfigurable metamaterial antenna. I have demonstrated that this model is able to more faithfully predict the far-field radiation pattern of an array than an ideal array factor model or a circuit equivalent model. Primarily, this improvement in accuracy is attributable to the fact that the DDA captures all first-order interactions between the waveguide field and the cells, simultaneously, whereas the other analytic models, the array factor and the circuit equivalent, do not permit such complete accounting of all these coupled physics.

The DDA possesses the qualities I identified as needing in a model: it consistently handles the length scales of the metamaterial, it is relatively agnostic to the geometric configuration of the cells in the plane, it naturally handles the individuality of the control of each cell,

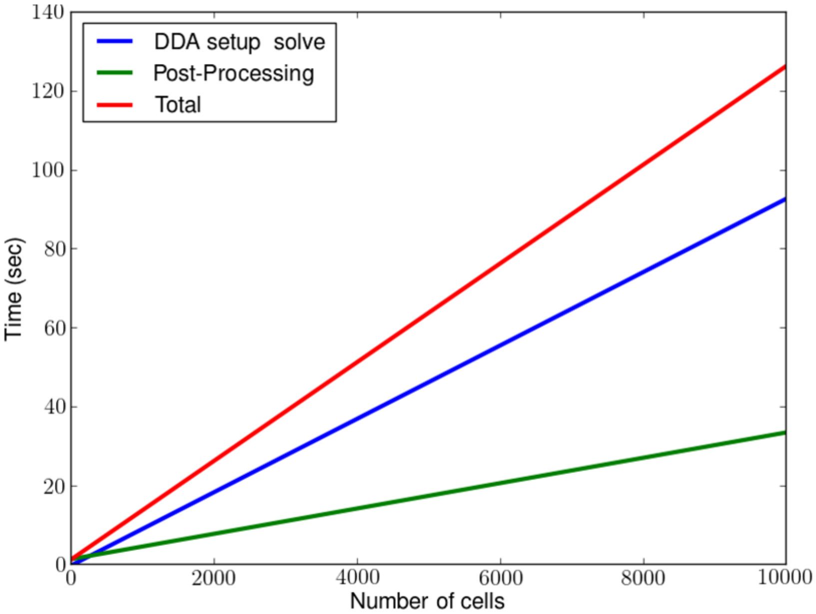

Figure 2.4: Computation time to compute the resulting far-field pattern of a metamaterial antenna using the discrete-dipole approximation model. The computation time to solve the DDA system grows linearly with the number of cells, making it much more attractive a modeling technique for large arrays than the most accurate numerical method, full-wave simulation.

it also naturally handles the waveguide fields, and it is capable of modeling a large array quickly. Besides these requirements, it has further benefits in that, for example, it actually efficiently leverages the accuracy of full-wave simulation to derive the necessary parameters for the model, and I have demonstrated that it is more accurate at predicting the antenna's far-field than other analytic models. The DDA model is an excellent tool to describe the metamaterial antenna behavior, and fulfills the requirement of the first step toward a self-optimizing metamaterial antenna as discussed in the introduction of this thesis. This tool allows me to next turn attention in chapter 3 to developing pattern synthesis techniques to obtain improved performance from the RHMA.

Chapter 3

SIDELOBE CANCELING PATTERN SYNTHESIS FOR A RHMA

3.1 Introduction

In chapter 2, I derived a fast, accurate, predictive model of the response characteristics of the metamaterial antenna that is capable of modeling both a variety of metamaterial antenna architectures and also any control pattern on a given architecture. In this chapter, I pursue pattern synthesis specifically for the RHMA. I examine how to suppress undesired far-field characteristics caused by the fundamental metamaterial response as well as by variations among individual antennas (e.g. due to manufacturing processes or other environmental factors).

While the RHMA solves the hardware problems of the incumbent technologies (the bulk and cost of gimballed dishes and phased arrays), it faces many of the same challenges as phased arrays in pattern synthesis and robust control during operation. For example, the RHMA must be able to scan without unacceptable levels of far-field radiation in undesired directions (sidelobes) that might interfere with other terminals or degrade the received signal. It is therefore mandatory to suppress the production of sidelobes while still preserving a strong main beam to track a given satellite. This can be done with software-defined optimal pattern synthesis - optimally defining, in real-time, the controls across all 10,000 cells to provide the best performance and lowest sidelobes. Software-based reconfiguration and control of the antenna has significant advantage over hardware-based beam-optimization because hardware is not at all mutable. On the other hand, software-defined control is nimble and can optimize across the myriad of conditions of the antenna, and it can be used to adaptively mitigate hardware variations. Also, software is easily and cheaply upgraded even after deployment of the antenna hardware. So, it is the aim of this thesis to derive and demonstrate an effective software-based pattern optimization scheme for the suppression of sidelobes specifically for the unique architecture of the RHMA. Yet, most work on metamaterial antennas has centered on the development of the hardware [33, 3, 42, 14] (and the references therein) with relatively little emphasis on pattern synthesis.

Thus far, metamaterial antenna literature points to basic phased array pattern synthesis theory [43], holographic theory [44, 45, 46, 47, 48, 49], leaky-wave antenna pattern synthesis [50, 51, 52, 53], and frequency selective surface synthesis procedures [54, 55, 56, 57, 58] to define its approach to pattern synthesis. Indeed, all of these approaches are related to each other and have elements relevant to the metamaterial antenna. However, as the hardware of each type of antenna is unique, so also must the synthesis technique be customized to work within the confines dictated by each antenna architecture and operating principle.

In this chapter, I utilize the predictive antenna model derived in the previous chapter to develop a pattern synthesis technique specific to the RHMA to optimize the far-field pattern, explicitly addressing particular sidelobes found in the RHMA radiation patterns. Within this chapter, section 3.2 describes the RHMA with special note of the characteristics of the antenna which feed into the pattern synthesis problem, and it also places the RHMA in the historical context of holographic antennas. In section 3.3, the theory connecting phased array pattern synthesis and holography is discussed. Section 3.4 briefly reviews prior work in sidelobe cancellation and then develops the algorithm useful to reduce specific sidelobes of the RHMA. Finally, in section 3.5, results demonstrating the efficacy of the algorithm on both the computational model of the system and on experimental hardware are demonstrated.

3.2 RHMA Physics for Pattern Synthesis

In this section, I give a brief historical perspective on the development of holographic antennas and the RHMA's place in that canon. I then again briefly describe the holographic metamaterial antenna physics to make special note of those properties that are particularly relevant to the problem of controlling the radiation pattern of the antenna.

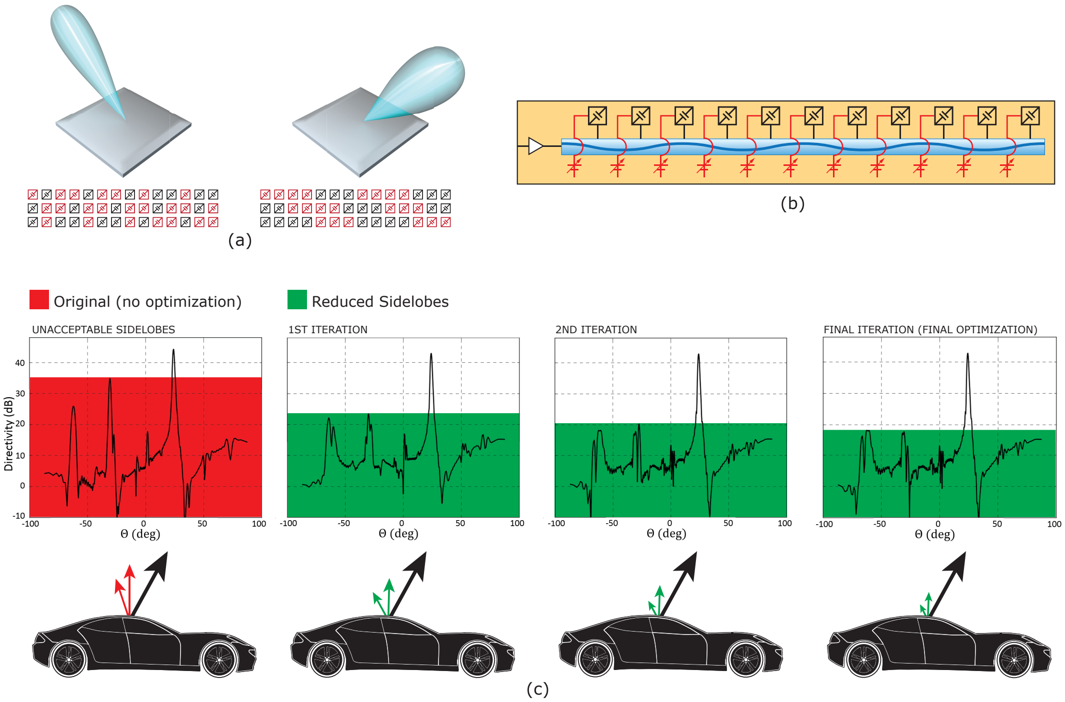

Figure 3.1: (a) Holographic images on the surface of the array, when illuminated by an underlying feed wave, produce a coherent beam. Different images, encoded in the array by the control applied to each unit-cell, produce beams in different directions. (b) The physics of the metamaterial antenna. The input carrier wave traverses the waveguide, and the unit-cells couple energy out of the feed. Further, the cells produce simultaneous amplitude and phase shift as a function of their control. (c) (Top row) Simulated far-field results of the algorithm iteratively targeting different sidelobes while continuously creating a main beam in the direction of 25.7° θ. (Bottom row) Representation of the simulated results in a mobile application.

3.2.1 Holographic antennas

A holographic interference pattern at microwave frequencies was first recorded at Bell Labs in 1950, but was only used for imaging rather than for attempting to reproduce the three-dimensional image, much less form a microwave-frequency beam [45]. It was not until 1970 that a microwave holographic antenna was first demonstrated by Checcacci, Russo, and Scheggi [44]. Particularly interesting in Checcacci's work is that their first interest beyond creating a beamforming antenna was to reduce or eliminate the “zeroth order” aberrations in the holographic image. They do not call these aberrations sidelobes, although that is what they are. They understood these aberrations to be errors in the holographic recording and addressed them accordingly, varying the approximation (pixelation and quantization) of the holographic recording to reduce this zeroth order. In this chapter, I address the sidelobes rather differently with a more complex pattern synthesis solution; however, their observations on the recording errors in holographic antennas provides further insight into the means of improving the RHMA pattern synthesis.

Holographic antennas have been under development more intensely since the early 2000’s since new materials better suited to the recording of radio frequency holograms have been increasingly available. There have been several disparate approaches to realizing efficient holographic antennas, these include static artificial impedance surfaces [59, 60, 61], passive leaky-wave holographic antennas [62, 63, 54] (and the references therein), reconfigurable artificial impedance surfaces [64, 58, 65, 66], and reconfigurable metamaterial antennas [67, 68] (the technology for which the sidelobe reduction method is developed). This literature on holographic antennas, heretofore, focuses on designing and improving the hardware devices that can accomplish the recording and illumination of a microwave hologram. These works have only gone so far in pattern synthesis as to demonstrate an active scanning capability in software. Optimization of the beam in the sense considered and demonstrated here - invasive manipulation of the characteristic radiation pattern - has not been discussed. This work on optimal holographic pattern synthesis is unique, and a significant advancement, for the holographic antenna.

3.2.2 RHMA physics for pattern synthesis

There are several interesting characteristics specific to the RHMA that directly affect the patterns that can be realized. First, a metamaterial antenna capable of closing a link with a satellite must have enough surface area to attain high enough gain. To achieve this basic performance requirement, the antenna is composed of more than 10,000 continuously and individually controlled unit cells, as mentioned previously. Also, I noted in the previous chapter that the vast number of controls and the high-degree of redundancy - meaning that one can point the main beam in the same direction with many different control patterns - is necessary to give the RHMA the flexibility for a broad electronic-scan range. Yet, it is impractical and infeasible to try random controls, e.g. a genetic algorithm, in search of good control patterns. There is, however, a small manifold within this massive parameter space that yields a coherent beam. The explication of the algorithm in section 3.4 specifically points out this useful (and unsurprising) low-dimensional parameterization that permits defining excellent control patterns quickly.

Apart from the large number of cells, each cell responds nonlinearly in both phase and amplitude to its control. The cells do not display *independent* amplitude and phase modulation as a phased array would, but instead are resonant; the amplitude and phase shift happen simultaneously as the control is changed. The resonance behavior, particularly the phase shift from the underlying carrier wave, is especially sensitive to manufacturing tolerances. Naturally, one seeks an optimization algorithm that is flexible and robust to such real-world tolerances. The need for flexibility in the face of uncertainty points toward an iterative algorithm where the antenna can learn about itself to improve its control pattern intelligently with feedback.

Since all cells of a row are fed by a single waveguide, all the elements *simultaneously* interact with and slightly perturb the feed wave based upon the controls themselves: upstream elements couple energy out so that downstream elements have less energy exciting them. Downstream elements incite a small backward propagating wave that is typically evanescent, but the elements are closely spaced so that even an evanescent wave may affect near neighboring cells. The coupling to the feed wave of each cell is dependent upon its control value. This complex simultaneous response will be demonstrated, theoretically, to be an important aspect to an accurate definition of the holographic image. A schematic description of these complex coupled physics of the array is shown in Figure 3.1(b). This image shows the traveling feed wave and the cells coupled to the waveguide. It also indicates the phase shift from the underlying carrier phase due to the resonance of the cells. This structure in which all cells are coupled to the waveguide as well as to each other and in which the phase shift is dependent on the control poses significant challenges for control and optimization.

3.3 Theoretical Pattern Synthesis Developments

In this section, two perspectives are given on the beamforming of the RHMA. First, I discuss the beamforming from the phased array perspective based upon the array factor, i.e. the summation of the fields radiating from each individual cell. Next, I explore beamforming from a holography viewpoint and highlight where the two interpretations connect. Particular attention is given when the mathematical theory sheds light on important considerations for the production of sidelobes and for optimal pattern synthesis to improve the radiated pattern.

3.3.1 Array theory development

The following is a short derivation of the basic control theory for a metamaterial antenna based upon familiar mathematical concepts from phased array theory. As noted in the previous chapter, equation 2.5, for the far-field of a collection of point dipoles, the far-field of an array of point sources is given by the array factor:

$$AF(\theta_0, \phi_0) = \sum_{n=1}^{N} A_n \exp(-i\mathbf{k}_f(\theta_0, \phi_0) \cdot \mathbf{r}_n), \tag{3.1}$$

where $\mathbf{k}_f(\theta_0, \phi_0)$ is the desired directional complex propagation vector in free space, and $\mathbf{r}_n$ is a coordinate of a radiator on the surface of the antenna. A_n are the complex weights of the individual antennas comprising the array. In a classical active phased array, both the amplitude and phase of these coefficients can be selected to achieve a desired far-field pattern. In the metamaterial antenna, the unit cells are resonant strctures and these properties cannot be independently selected. Yet, since phase shifters are not being used, the power needed to steer the antenna is 1/100th or better than that of a phased array.

The phase of the resulting complex weight in the metamaterial antenna is largely the result of two effects, namely the traveling wave phase and the additional phase shift from the base traveling wave phase induced by the resonant properties of the cells, refer to the model in figure 3.1(b). Thus the phases of the A_n are constrained variations around the traveling wave phase. The achievable amplitude range between "off" (minimally excited cell) and "on" (maximally excited cell) is limited to values as small as 1:3 or up to about 1:15 for the RHMA. One can think of the selection of the A_n as being a severely constrained version of a phased array, or one can think of them as a holographic recording mechanism as described in the next section.

As is well-noted, the far-field is related to the array weight distribution by a Discrete Fourier Transform. One seeks to create a delta function of the energy in a particular direction in the far-field, aligning the phase distribution attained from the traveling wave with the desired radiating phase distribution:

$$\sum_{n=1}^{N} \mathbf{E}_n(\mathbf{r}_n; \mathbf{k}_s) \propto \delta(\mathbf{k}_f(\theta_0, \phi_0) - \mathbf{k}_s), \tag{3.2}$$

where $\mathbf{k}_s$ is the complex propagation vector of the reference traveling wave, $\mathbf{E}_n(\mathbf{r}_n; \mathbf{k}_s)$ is the electric field generated by a radiator at location $\mathbf{r}_n$, and δ is the Dirac delta function.

If the array were infinite and a continuous current distribution, the Fourier analysis indicates that the distribution of the weights should then be:

$$A(\mathbf{r}) = \exp(-i\mathbf{k}_f(\theta_0, \phi_0) \cdot \mathbf{r}) \exp(i\mathbf{k}_s \cdot \mathbf{r}). \tag{3.3}$$

Note that these ideal weights are complex, and one must apply real controls to approximately achieve these desired weights. Additionally, given the assumed phase distribution on the array $\exp(i\mathbf{k}_s \cdot \mathbf{r})$, some cells will be displaying exactly the correct phase indicated by equation 3.3 while most of them will be radiating a phase which is incorrect, at the extreme case, being 180° out of phase. A control strategy may then be to allow cells at the correct phase to radiate strongly and to disallow cells at the incorrect phases to radiate. Recall that this is accomplished by tuning the location of the resonant frequency of the cell nearer to or further from the operating frequency. This strategy is parameterized to control values between “off” and “on” or $[0, 1]$ as:

$$m(\mathbf{r}_n; \theta_0, \phi_0) = \frac{\Re(A_n) + 1}{2}. \tag{3.4}$$

This real-valued control is a shifted and scaled cosine wave, $\cos((\mathbf{k}_s - \mathbf{k}_f(\theta_0, \phi_0)) \cdot \mathbf{r})$. A depiction of sinusoidal control patterns producing different beams is shown in Figure 3.1 (a). Control patterns of different period produce different beams as indicated by equation 3.4.

Understanding the Fourier Transform relationship between the distribution on the surface of the antenna, partly achieved by the application of the cosine-wave control, and the far-field of the array point to some fundamental causes of sidelobes. First, the antenna is of finite size. The Fourier spectrum of the finite distribution sets the beamwidth of the mainbeam, and it also sets the width and spacing of the Gibbs oscillations induced by discontinuity at the edges of the array. The discontinuity at the edge of the array is why classical tapering functions, such as cosine, binomial, and Taylor n-bar, reduce sidelobes; they taper the amplitude of radiation of the array near the edges such that there is not such an abrupt discontinuity inducing high sidelobes. Yet, these tapers effectively reduce the size of the aperture, and so increase beam width [69, 70, 71, 72, 73, 74].

Secondly, the pixelation of the array due to having a finite number of radiators spaced some distance part yields a sampling of the ideal continuous cosine wave. This is even neglecting the fact that the resonant behavior of the cells means that one is not exactly sampling the ideal wave. The well-studied relationships of the Discrete Fourier Transform hold for the discretized antenna array indicating that sampling the waveform induces sidelobes due to aliasing of the cosine control pattern. In fact, harmonic sidelobes of the form $\cos(m \times (\mathbf{k}_s - \mathbf{k}_f(\theta_0, \phi_0)) \cdot \mathbf{r})$ with $m \in \mathbb{Z}^+$ are the largest lobes in measurement and simulation. The sidelobe suppression algorithm derived in section 3.4 is developed primarily to tackle these largest sidelobes created by harmonics in the modulation pattern, but the algorithm does not require knowledge of the cause of the sidelobe to operate.

3.3.2 Holographic theory development

Alternatively, one can consider the pattern synthesis problem from the holographic perspective and derive the same synthesis strategy. This second perspective is particularly helpful for identifying additional limitations of the above noted control strategy beyond the finite array size and the pixelation/sampling of the cosine waveform. The theory of holography is to encode on a surface (in this case, an antenna) an image such that, when the surface is illuminated by a specified reference wave, the viewer sees a complete version of the originally recorded 3D image. Refer to Figure 3.1(a).

In the case of a RHMA, consider the desired 3D image to be a spherical wave emitted by (or converging upon) a point source in the far-field (a satellite). This propagating wavefront appears as a plane-wave on the flat surface of the antenna on earth. The illuminating reference wave is the wave that lights up the metamaterial resonators: the propagating electric-field in the waveguide.

$$\begin{aligned} \Psi_{\text{obj}}(\mathbf{r};\theta_0,\phi_0) &= \exp(-i\mathbf{k}_f(\theta_0,\phi_0)\cdot\mathbf{r}) && (3.5) \\ \Psi_{\text{ref}}(\mathbf{r}) &\approx \exp(-i\mathbf{k}_s\cdot\mathbf{r}), && (3.6) \end{aligned}$$

where Ψ_{obj} is the desired far-field wave and Ψ_{ref} is the illuminating wave in the waveguide. In particular, I am interested in coordinates $\mathbf{r}$ that are on the surface of the antenna.

The *transmittance* represents the "picture" on the surface derived from the simultaneous presence (or summation) of the two waves.

$$\begin{aligned} T \propto |\Psi_{\text{obj}} + \Psi_{\text{ref}}|^2 &= |\Psi_{\text{obj}}|^2 + \Psi^*_{\text{obj}}\Psi_{\text{ref}} + \\ &\quad \Psi_{\text{obj}}\Psi^*_{\text{ref}} + |\Psi_{\text{ref}}|^2. && (3.7) \end{aligned}$$

T is proportional to the right hand side of this equation by a scalar (potentially complex value) indicating that small amounts of energy may be lost or dispersed by other mechanisms.

If this transmittance picture is "recorded" in some way, then lit up by the original reference wave, one obtains:

$$\begin{aligned} T\Psi_{\mathrm{ref}} &\propto |\Psi_{\mathrm{obj}}|^2\Psi_{\mathrm{ref}} + |\Psi_{\mathrm{ref}}|^2\Psi_{\mathrm{ref}} + \\ &\quad \Psi^*_{\mathrm{obj}}\Psi^2_{\mathrm{ref}} + \Psi_{\mathrm{obj}}|\Psi_{\mathrm{ref}}|^2. \end{aligned} \tag{3.8}$$

The four terms appearing in the imaging of the hologram represent different physical terms.

The first term $|\Psi_{\mathrm{obj}}|^2\Psi_{\mathrm{ref}}$ has amplitude proportional to the object beam and points in the propagating direction of the reference wave. This image does not show up in the hologram; its image and energy are transferred through with the reference wave. In the holographic antenna case, the energy in this portion of the image is transmitted down the waveguide and attenuated at the end. The second term is similar to the first in that it is in the direction of the reference wave and does not produce an image. The third term $\Psi^*_{\mathrm{obj}}\Psi^2_{\mathrm{ref}}$ produces an image of the conjugate to the desired beam. This image for the holographic antenna is not in the visible spectrum of the array, being a projection of the image behind the antenna. The fourth term $\Psi_{\mathrm{obj}}|\Psi_{\mathrm{ref}}|^2$ is the term of most interest. It has an amplitude proportional to the input wave, and it points in the direction of the desired object beam.

I will refer often to the wave interference as the portion of the transmittance which is desirable to capture:

$$\Psi_{intf} =: \Psi_{\mathrm{obj}}\Psi^*_{\mathrm{ref}}. \tag{3.9}$$

To get maximal energy transfer in this term, the interference image needs to be recorded correctly and the reference beam in the interference calculation needs to exactly match the illuminating wave Ψ_{ref}. Any errors in this image recording will cause the object beam to not be exactly replicated, invariably causing additional sidelobes.

For the metamaterial antenna considered here, there are a number of deviations from these ideal equations that will occur, just as noted before in the phased array theory. The finite size of the array limits the resolution of the image in the far-field which dictates, as the phased array theory noted, the width of the main beam, and reduce the field of view, which translates to the antenna as a limited scan range. The pixelation of the array also limits the resolution of the far-field, as noted before.

The other difficulty in pattern synthesis for the RHMA that is highlighted by the holographic perspective and that was not obvious from the array theory analysis, is that the reference wave in the wave interference and the illuminating wave need be exactly the same or there will be aberrations in the resulting holographic image. That is, if $\Psi_{\mathrm{illum}} \neq \Psi_{\mathrm{ref}}$, then the resulting transmittance term becomes:

$$\Psi_{\mathrm{obj}}\Psi_{\mathrm{ref}}\Psi_{\mathrm{illum}} \neq \Psi_{\mathrm{obj}}|\Psi_{\mathrm{ref}}|^2. \tag{3.10}$$

No longer is all the energy directed in the direction of the object wave. Unfortunately, with the resonant cells of the RHMA coupling to the feedwave and to each other depending on their control value, the application of the controls to the individual elements to record a desired interference image actually affects the illuminating reference wave enough to cause errors. This problem that the controls affect the illuminating wave is mitigated by an iterative machine-intelligent pattern synthesis optimization. An iterative, feedback-controlled approach permits the antenna to teach itself improved patterns.

Returning to the basic wave interference formulation for the RHMA, for a scan angle of (θ_0, ϕ_0) this interference equation is given by:

$$\Psi_{intf}(\mathbf{r}; \theta_0, \phi_0) =: \exp(-i\mathbf{k}_f(\theta_0, \phi_0) \cdot \mathbf{r}) \exp(i\mathbf{k}_s \cdot \mathbf{r}) \tag{3.11}$$

It is obvious, but worth note, what has been achieved in the holographic and phased array theories. The problem one initially faces with the RHMA is to specify a control value at each of 10,000 cells simultaneously to form a coherent beam. The holographic wave interference equation gives one the control for each cell with just a few parameters (pointing angle and propagation constants). Having only a few parameters to keep track of and optimize is a boon for pattern storage and optimization. A handful of parameters are much easier to optimize in real-time than tens of thousands.

Also, note that this wave interference equation derives exactly the same weighting and control strategy as was found in the array factor analysis equations 3.3 and 3.4. But this derivation gives additional understanding of the potential for sidelobes in the resulting far-field as coming from a mismatch of the reference wave used for calculation of the control and

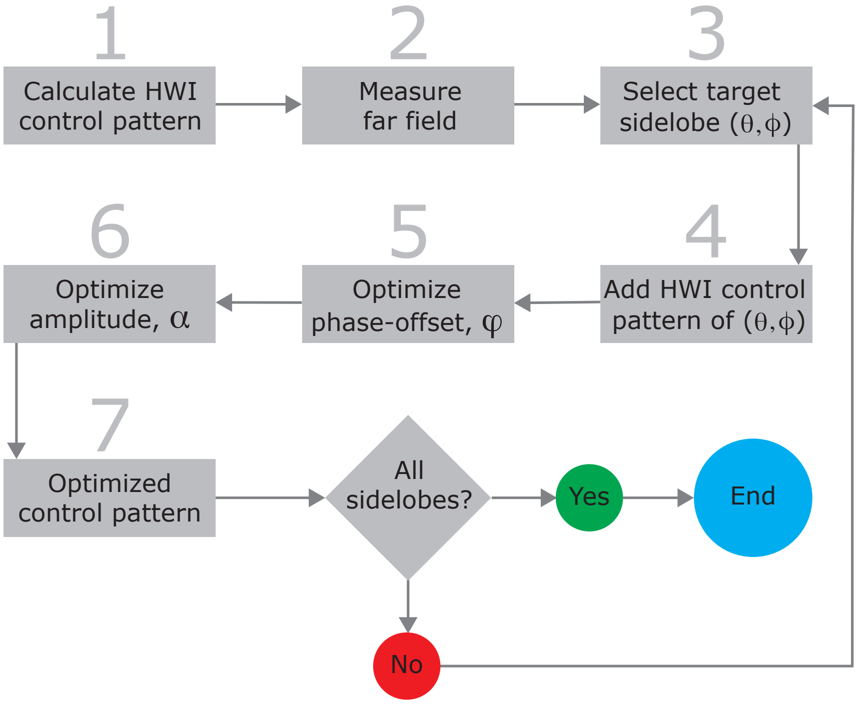

Figure 3.2: Flowchart of sidelobe reduction algorithm. HWI stands for Holographic Wave Interference, see equation 3.9.

the reference wave that actually illuminates the array due to the application of the controls themselves.

In the next section, I leverage the low-dimensional parameterization of the antenna control pattern, along with an iterative optimization approach to mitigate recording errors, to define a new pattern synthesis technique that effectively reduces the sidelobes of the RHMA.

3.4 Sidelobe Canceling Pattern Synthesis Algorithm

In this section, I develop an algorithm for finding optimal control patterns for the RHMA that reduces targeted sidelobes, but first, I briefly review the historical work in sidelobe cancellation for traditional digital beamforming.

3.4.1 Sidelobe cancellation in arrays

Sidelobe cancellation has a rich history in the academic literature as well as in practice. Several patents were issued for device configurations for sidelobe cancellation in the mid-1960's [75, 76, 77, 78]. Unlike the operating principles of the metamaterial antenna, these patents dictate the use of spatially separate arrays for receiving the signal and for detecting the noise signals. During the processing of the signal, the interference signal is subtracted from the reference, and thus the unwanted information received from sidelobes is suppressed.

The mathematics of this interference-signal-subtraction approach was formalized in the Generalized Sidelobe Canceler that was published in 1975 by Widrow et al. as an application of a broadly-useful adaptive noise canceling algorithm [79]. The algorithm dictates how to optimally tune the weights of a receiving digital beamformer or phased array during signal processing to remove the interference signal and minimize the loss of the desired signal. More theoretical analysis and extensions to the generalized sidelobe canceler were forthcoming after Widrow. Other extensions and examinations of this method which added complexity and increased robustness or efficiency, but did not represent significant departures in approach or application, include increasing computational efficiency by manipulation in the frequency domain [80, 81, 82, 83, 84, 85]. Yet, all these extensions still assume that the signal from each antenna comprising the array is separable, which is not the case in the holographic antenna.

The current work develops a sidelobe cancellation algorithm that works under the same principle as the noise-canceling algorithm of Widrow et al., but with important and non-intuitive extensions needed for the RHMA. The Generalized Sidelobe Canceler operated on signal summation; the RHMA sidelobe cancellation instead operates on pattern summation.

3.4.2 RHMA sidelobe canceling pattern synthesis

The sidelobe targeting pattern synthesis approach starts from the control strategy that was derived in section 3.3 and is given in equation 3.4 to be a discretized cosine wave, step 1 in

Figure 3.2.

Recall the initial control pattern for an array scanning to the angle (θ_0, φ_0) is:

$$\begin{aligned} m(x_n;\theta_0) &= \frac{\Re(\Psi_{intf}(x_n;\theta_0,\varphi_0))+1}{2}, && (3.12)\\ &= \frac{\Re(\exp(-i\mathbf{k}_f(\theta_0,\phi_0)\cdot\mathbf{r})\exp(i\mathbf{k}_s\cdot\mathbf{r})+1}{2}, && (3.13)\\ &= \frac{\cos(i(\mathbf{k}_s-\mathbf{k}_f(\theta_0,\phi_0))\cdot\mathbf{r})+1}{2}. && (3.14) \end{aligned}$$

The pattern synthesis approach to reduce any particularly high-energy sidelobe is to destructively interfere a second "main beam" with the targeted sidelobe. This is done by mangling the original single-tone cosine control wave, superimposing an auxiliary control pattern, to produce the image of the sidelobe that is 180 degrees out of phase with the targeted sidelobe - cancelling the targeted sidelobe. The effect in the cosine control wave will be a two-toned (or multi-toned if more than one sidelobe is targeted) control waveform. Refer to figure 3.3 for a graphic representation of this pattern summation approach.

The parameterized control pattern which reduces a sidelobe at a given angle (θ_1, φ_1) is a renormalization of the weighted sum of the original control pattern and the auxiliary control pattern:

$$\begin{aligned} m_{sum}(x_n;\theta_0) &= \cos(i(\mathbf{k}_s-\mathbf{k}_f(\theta_0,\phi_0))\cdot\mathbf{r})+ && (3.15)\\ &\quad \alpha_1\cos(i(\mathbf{k}_s-\mathbf{k}_f(\theta_1,\phi_1))\cdot\mathbf{r}) \end{aligned}$$

Then m_{sum} is normalized such that $0 \leq m_{sum} \leq 1$ for all x_n as before, see steps 2-4 in figure 3.2.

I noted previously that the wave interference equation gives a low-dimensional manifold in parameter-space that yields coherent beams and that the high-degree of redundancy in the 10,000 cell controls could be used to improve the beam pattern. To address sidelobes, my algorithm consumes some of the redundant degree of freedom by adding a second waveform, found on the same low-dimensional manifold, but with two additional parameters per targeted sidelobe.

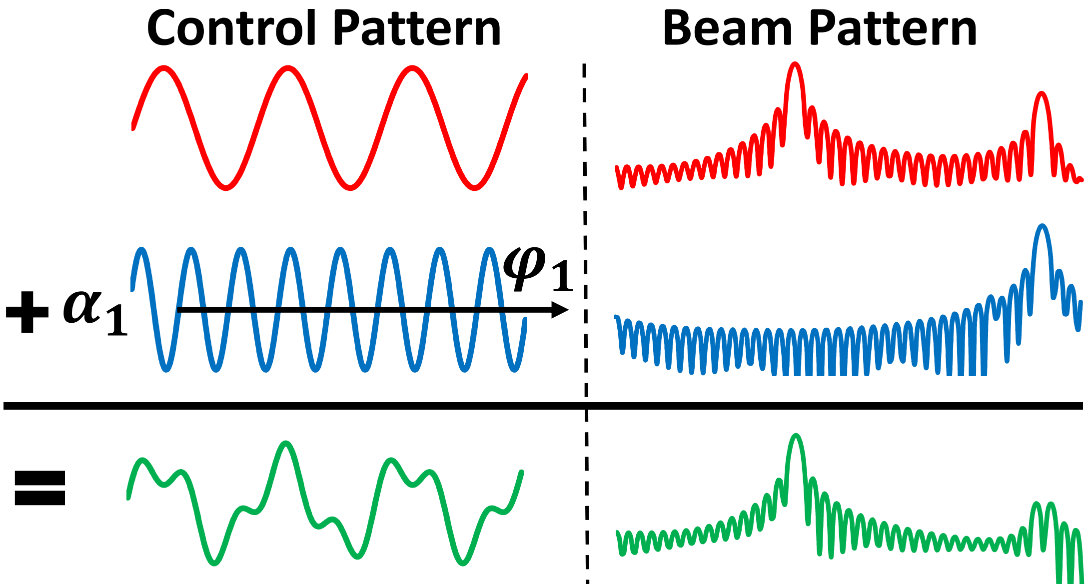

Figure 3.3: Sidelobe cancellation with holographic pattern synthesis approach. (Left) A sketch of two control patterns summing with a weight factor and phase-offset to produce the third (bottom) control pattern as per equation 3.16. (Right) The representative beam patterns generated by each control pattern on the left. The second beam pattern (middle) cancels the sidelobe from the original pattern (top) to produce an improved beam pattern (bottom).

The two parameters to be optimized are an amplitude, α_m, and a phase-offset, φ_m, see steps 5 and 6 of Figure 3.2. The phase-offset must be correctly defined such that the newly produced lobe is 180° out of phase with the original sidelobe while the amplitude must be selected to sufficiently reduce the sidelobe. However, both parameters may have a detrimental effect on the main beam and a trade-off in main beam gain and sidelobe reduction may have to be made.

With these two additional parameters parameters in addition to the scan angle (θ_m, φ_m) for each of the M auxiliary cosine waveform control patterns that are added to target M sidelobes, the total parameters that define the control patter are $2+4M$, and the parameters that must be optimized are still just $2M$. Significantly, optimization can simply be performed much more quickly with fewer variables to identify.

To optimize the parameters, in this chapter, I use an alternating gradient-based approach. I iterate between optimization of the phase variable with the amplitude variable held fixed and optimization of the amplitude variable with the phase variable held fixed. When optimizing a single parameter, I use a back-tracking line search based on a numerical gradient (I refer to this as a *gradient based back-tracking line search* or GB-BTLS). That is, to optimize a variable, I apply two different patterns with the variable in question slightly different between the two patterns. From these two patterns, a gradient with respect to the parameter change is obtained. Then, a back-tracking line search is used to find the optimal step-size based on the computed gradient. After following this gradient direction to its best point, another gradient is computed and another line-search followed to optimal. When optimization in this way stalls for one variable, the algorithm switches to following the same procedure on the second variable. In this way, the algorithm alternates between optimizing the two variables until further improvement is not being made.

To ensure that the gradient-based approach will converge, I investigated the parametric topology when maximal reduction of the targeted sidelobe is the optimization criteria. This parameter space is smooth with respect to each parameter independently. That is, fixing one parameter, the sidelobe level varies smoothly with the second parameter. Figure 3.4 shows two representative curves. On the left of Figure 3.4, I show the sidelobe level when the phase-offset of the auxiliary pattern is fixed (at 2°) and the amplitude is varied from 0 to -1; the sidelobe level varies smoothly and has a single minimum. Similarly, the right plot of the figure shows smooth variation of the sidelobe level when the amplitude of the auxiliary pattern is fixed at -0.27 and the phase is varied through all 360 degrees.

The phase and amplitude are well-behaved, ensuring that the gradient-based approach is successful, and the parameters could be directly analytically defined if the system were simply a phased array obeying simple linear physics. However, there are many places where the linear assumptions break down and many opportunities for real-world errors to significantly deviate from the answer indicated by analytic modeling, including from build tolerances, inexact characterization, inexact modeling, and the application of the controls themselves

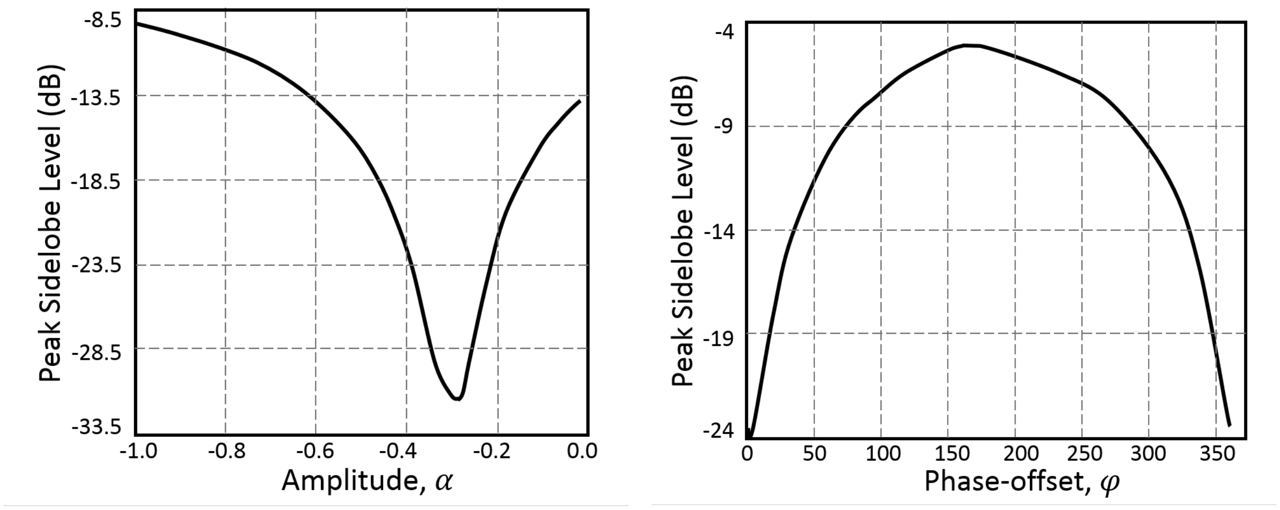

Figure 3.4: Sidelobe level as a function of (left) amplitude of auxiliary pattern and (right) phase-offset of auxiliary pattern for the example of an array pointing at $-30°$ and targeting a sidelobe at $+4°$.

affect the resultant far-field. Also, as previously noted, the fact that the controls affect the illuminating wave, also makes an iterative approach requisite. Because of all of these difficulties, one must pursue an iterative, feedback-driven optimization approach to pattern synthesis. In the next chapter, I go further to introduce a time-varying element to the antenna's condition and behavior. These additional concerns of dynamic operation require an adaptive algorithm to continually synthesize good patterns for the antenna, no matter what environment it might be experiencing or what objective it is needing to pursue at the moment.

3.5 Sidelobe Canceling Pattern Synthesis Results on a RHMA

Results are presented in this section using the pattern synthesis with optimization approach of section 3.4 both in simulation on a DDA modeled single-channel, 260-cell Ka-transmit-band antenna. The antenna operates at 30GHz and the unit cells have a tuning bandwidth of approximately 10%. The operating frequency is above the highest resonant frequency of the unit cells. The simulated antenna also has a hardware taper such that cells at the beginning and end of the array scatter less energy from the waveguide than cells in the center (as mentioned in section 3.3, a taper reduces sidelobe levels due to the discontinuity of energy at the edges of the finite antenna). Results are also presented from measurement of an experimental device. This antenna is a smaller, 96 cell single-strip aperture, also operating in the Ka-transmit-band with similar cell tuning response to the simulated antenna. This antenna, however, does not have a designed hardware taper. These results show the ability of the algorithm to iteratively and significantly reduce undesired sidelobes while not degrading the rest of the far-field pattern, particularly, the main beam gain is acceptably maintained.

3.5.1 Computational results

Part (c) of figure 3.1 shows iterative sidelobe targeting for the 260-cell single-strip antenna simulated with a DDA model. The main beam points to 25.7° θ, and the algorithm iteratively reduces 5 sidelobes at -31.1, -62.0, -64.6, -27.9, and -60.3 degrees, in that order, though the figure only shows the first and last of these iterations. It reduces each of these sidelobes by 17.62 dB, 3.98 dB, 4.43 dB, 8.92 dB, and 1.87 dB, respectively. The algorithm successfully improves the original pattern whose first sidelobe was only 8 dB down from the main beam, and produces a pattern where all sidelobes are more than 22 dB down. It is worth note, that these targeted sidelobes were induced by harmonic content in the control pattern caused by the resonant, phase-shifting nature of the metamaterial unit cells. However, the algorithm does not need to identify the cause of the sidelobe for it to achieve reduction.

Part (c) of figure 3.1 also shows a physical representation of what these antenna patterns mean, conceptually, in a mobile use-case. The antenna is placed in the roof of a vehicle, and the arrows show where the primary energies of the antenna are being radiated. As the algorithm progresses through sidelobe targeting, the sidelobes shrink rapidly until one is left mostly with just a main beam in the desired direction. The antenna is no longer at risk of interfering with other satellites' transmissions nor at risk of receiving unacceptable levels of noise making the anticipated transmission impossible to read.

Note that the addition of another discretized wave to the surface of the array may create new sidelobes, depending on the sidelobe pattern of the auxiliary pattern itself. However, the amplitude of these new lobes will be small since the additional pattern will be added in "small doses" compared with the original pattern. It is even sometimes the case that some of these added sidelobes cancel out (or reduce) other pre-existing sidelobes leaving one with a further improved antenna pattern.

3.5.2 Pattern synthesis impacts on gain

The sidelobe-canceled pattern will have reduced gain in the main beam as small amounts of the controlled energy are being redirected to point in the direction of the sidelobe. However, this reduction will be slight in comparison to the large drop in sidelobe amplitude since the original control waveform will still dominate the auxiliary pattern. Yet, the addition of more and more auxiliary patterns on top of the original waveform will redirect more and more of the energy away from the main beam.

Figure 3.5 shows the gain reduction as a function of the number of sidelobes killed-off for several trials of the algorithm on the DDA modeled antenna strip. The figure also shows the accompanying reduction in the sidelobe level. The gain drops significantly with the first targeted sidelobe and then degrades more slowly as additional sidelobes are targeted. This is due to the fact that the first sidelobe targeted is the largest, and the amplitude α_1 which is optimal to reduce this sidelobe is much larger than the amplitude necessary for the other smaller sidelobes. Thus, with the first, large sidelobe, the auxiliary pattern skews the primary pattern much more heavily than any subsequent addition. Note, however, that the gain reduction is significantly less than the improvement in the sidelobe level.

3.5.3 Experimental results

Figure 3.6 shows the results of using this algorithm on an experimental antenna. The antenna is intended to scan to broadside (0° θ), and the first two sidelobes, first -4° and then $+5^\circ$, are reduced with the algorithm. These sidelobes, unlike the previously modeled antenna,

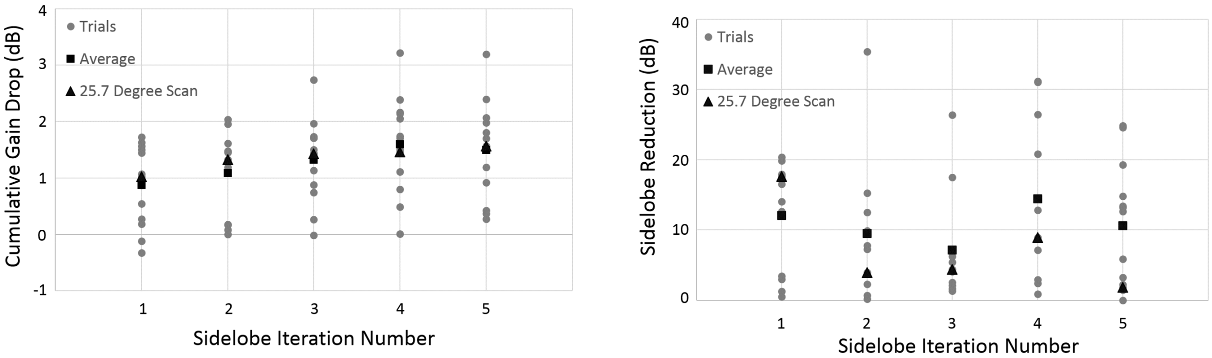

Figure 3.5: (Left) Cumulative reduction in peak gain (dB) and (right) sidelobe reduction (dB) as a function of the number of targeted sidelobes over 13 trials at equally spaced scan angles between −30° θ and +30° θ with the average reduction (square) and the reduction for the scan angle 25.7° with complete results shown in Figure 3.1 (d) (triangle). The gain reduces most substantially with the first targeted sidelobe while the reduction in sidelobe energy is significant for all targeted sidelobes.

are not caused by harmonics in the control pattern since those types of sidelobes are not in the visible spectrum of this little antenna at broadside. Yet still, the −4° sidelobe was reduced by approximately 8 dB and the +5° sidelobe was reduced by approximately 6 dB. Note that the rest of the pattern is relatively unperturbed, and in some place is noticeably improved even though those sidelobes were not targeted. Also, note that after the −4° lobe is targeted, the +5° sidelobe correction did not alter, and particularly it did not degrade, the −4° sidelobe improvement by much. Since the modulation patterns are independent, they do not perturb the pattern over-all, only in specific places, those places in their own spectrum where large sidelobes may appear.

The results of implementing the sidelobe cancellation algorithm developed in section 3.4 for the RHMA on both a simulated antenna and an experimental device demonstrate the great efficacy of this pattern synthesis and optimization approach to reduce unwanted sidelobes of the metamaterial antenna. This technique is flexible enough to target multiple sidelobes on antenna platforms of different size and design (e.g., one with a hardware ta-

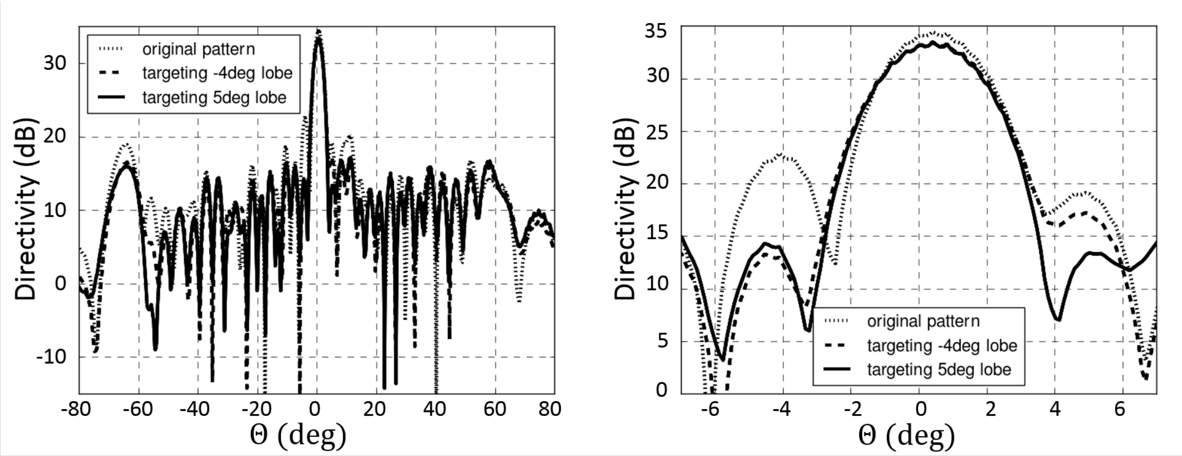

Figure 3.6: Measured results from a 96 cell single-channel aperture. The aperture was scanned to 0° θ and the algorithm was used to reduce the first two sidelobes at $-4°$ (reduced by ≈ 8 dB) and $+5°$ degrees (reduced by ≈ 6 dB). (Left) Entire visible angular region and (right) enlargement of the main beam and targeted sidelobe region.

perand one without). The pattern synthesis reduced the targeted sidelobes on both apertures despite being in different locations, and having different causes - the sidelobes targeted in simulation were harmonic sidelobes while the sidelobes of the hardware antenna are due to other causes, either manufacturing related or due to not having a taper, because harmonic sidelobes are not in the visible spectrum of this antenna when scanned to broadside.

Summary

This chapter introduced a pattern synthesis technique for the RHMA to improve the RHMA's far-field pattern by reducing specific sidelobes. It provided background on basic pattern synthesis for the RHMA from both the phased array analysis and the holographic recording analysis. The two perspectives give insight into the various causes of sidelobes, which helps point toward pattern improvements specifically for the RHMA. For example, I pursued an iterative approach to optimizing the synthesized pattern because one sees that the application of the controls affects the illuminating wave, and thus, an analytic answer based on linear array theory would not yield optimal solutions for the RHMA.

After the theoretical development, I derived a synthesis approach to reduce sidelobes by adding two waveforms together to cancel a targeted sidelobe. The pattern synthesis approach was successfully demonstrated to significantly reduce sidelobes and maintain main beam gain for both a modeled system and in experiment. This demonstration is an important achievement because it could not have been expected that simple linear superposition of patterns would be effective at all when contending with the complex, non-linear, and tightly-coupled physics of the RHMA. Also of significance in the demonstration is the fact that the optimization algorithm was successful on a manufactured device - following the algorithm, not simply applying a pattern resulting from optimization in simulation, achieved notable success in practice.

This is a second, substantial step toward an adaptive metamaterial antenna. In the previous chapter, I derived a model to accurately predict the pattern of the RHMA to be able to test pattern synthesis approaches to improve performance, and in this chapter, I used that model to derive a pattern synthesis technique that specifically targets the characteristics of the far-field pattern of the RHMA. In the next chapter, I take the final step toward an adaptive RHMA - synthesizing optimal patterns for the antenna live, during operation, with feedback control.

Chapter 4

EXTREMUM-SEEKING CONTROL OF A RHMA

4.1 Introduction

In the previous chapter, I introduced a pattern synthesis approach, to optimize the antenna pattern, eliminating certain sidelobes from the resulting far-field pattern of the RHMA. This synthesis method was capable of finding a set of unit cell controls to suppress certain sidelobes in a static, tuning, or off-line optimization situation - one in which there is no measurement noise and the conditions under which the antenna is operating are not changing.

Yet, the pattern synthesis theory is not enough for continuous, dynamic operations outside of the controlled factory environment. A machine-intelligent, dynamic controller is required to achieve and maintain high performance of the RHMA. This includes maintaining high gain, reducing sidelobes, and mitigating interference while the antenna is operating in changing environmental conditions (wind, rain, temperature, dust, movement, vibration, etc.) and in the presence of real-world errors in measurements (noisy measurement of signal strength, errors in position estimation, etc.). For the metamaterial antenna, the topic of feedback control is uncharted. In this area, the promise of the RHMA for robust, no-human-intervention, low-maintenance, high-throughput communications in mobile applications has rested on the possibility of leveraging adaptive array techniques (of which there is a vast amount of literature) to provide answers for dynamic, electronically-reconfigurable beam optimization.

The algorithmic infrastructure I present in this chapter demonstrates that the implementation of an extremum-seeking controller is capable of meeting the dynamic operational requirements of the RHMA. Specifically, it can perform continuous optimization of an RHMA by using the pattern synthesis approach for sidelobe cancellation presented in the previous chapter. It also continuously maintains an optimal solution state even when subjected to measurement noise and dynamically changing antenna conditions. In this chapter, I also introduce and evaluate an objective function that is measurable during operation, and I investigate the effect of the objective function on both the controller and beam performance. Finally, I demonstrate a way to speed-up the time-to-optimality that is extraordinarily robust to measurement error and that is based on the optimal control concept of value function approximation [86]. As an overall algorithmic package, the mathematical framework provides a robust, machine-intelligent architecture capable of enabling the RHMA technology.

This chapter is organized as follows. In section 4.2, I discuss and implement the multivariable extremum-seeking controller for dynamic pattern synthesis, demonstrating its effectiveness in several real-world problems. In section 4.3, I explore different optimality criteria to find an objective function which provides the final pattern synthesis that is desired, amenable to the ubiquitous feedback constraints when operating in a dynamic environment, and works well with the controller. Finally, in section 4.4, I develop a more exotic approach to speed up the controller's convergence based upon value function approximation. A summary is provided in section 4.4.

4.2 Adaptive Pattern Synthesis via Feedback Control

4.2.1 Background in adaptive arrays

There is a veritable ocean of work in adaptive antenna arrays and optimal digital beamforming in the literature with whole conferences dedicated to the topic. Many large tomes have been produced on the topic including [87, 88, 89, 90]. With so much literature, it is impossible to review it all, and, as might be expected with such an ever-expanding body of work, the term "adaptive antenna arrays" is used to refer to a variety of areas of work. Largely, the term refers to algorithms to modify the controls of the constituent antennas of an antenna array to change the far-field pattern of the array to achieve, as fully as possible within the confines of the antenna capabilities, some desired far-field characteristic such as maximizing gain, suppressing sidelobes, null-steering, and beam-tailoring. Yet, again, the literature on adaptive arrays is so broad that the term also encompasses algorithms to change the controls to, in fact, *minimize* changes in the far-field while achieving more desirable power-consumption characteristics, as just one example of the myriad of concepts encompassed by the "adaptive array."

The broad definition of the adaptive arrays within the literature blurs the lines between pattern synthesis and feedback control thereof, as it does both, simultaneously. For example, there are model-based techniques which define the pattern synthesis approach based on the model of the antenna and then layers on an optimization approach (either direct solution, if the model is particularly straight-forward or gradient-based, otherwise) in much the same way I layered the GB-BTLS optimization onto the holographic sidelobe-canceling pattern synthesis approach in the previous chapter. These model-based synthesis methods include convex optimization [91], conventional beamforming, optimal beamforming, beam-space processing, optimization using reference-signal, frequency domain beamforming, and the eigenstructure method [92, 93, 94]. For optimization with these synthesis techniques, common methods include sample matrix inversion (SMI) [95], least mean squares (LMS) [96, 97], alternating projections [98], the constant modulus algorithm (CMA) [99], and conjugate gradient (CG) [100]. However, these methods are not helpful in this situation for two reasons: the pattern synthesis approach they advocate is not applicable to the RHMA because they are generated by different antenna operating principles, and then their optimization approaches suffer the same deficiencies as my own gradient-based approach.

On the opposite end of the spectrum is the other popular class of techniques in the adaptive array literature that completely bypasses both the issues of a model-based pattern synthesis technique and a gradient-based optimization based on that pattern synthesis approach to, again, affect simultaneous pattern synthesis and feedback control. These non-parametric methods include genetic algorithms [101, 102, 103], particle swarm [104, 105, 106], and neural networks [107, 108, 109]. Non-parametric methods make no assumptions about the antenna, simply applying control inputs (in phased arrays, these are antenna weights), measuring the output (the far-field and derived objective function value), and then adjusting the inputs semi-randomly according to each method's adaptation principles in search of improving objective function performance. These methods are flexible and robust. However, they are only acceptable for off-line optimization when there are many control inputs (for example, in the case of the metamaterial antenna, the control of more than 10,000 individual cells) or for on-line optimization of 10's or, perhaps, 100's of control variables. However, these non-parametric methods are not advantageous in this situation as I already have a pattern synthesis approach in mind, so I have no need of randomly varying controls of all the cells. Also, I know that the topology of the objective function is well-behaved (amenable to gradient-based optimization), so a non-parametric method would be inefficient compared to a standard controller.

While I am trying to achieve the same ends as the adaptive array antenna literature, its approaches cannot fully solve the problem of continuous control of the beam pattern of the metamaterial antenna. Having selected the pattern synthesis approach based on the holographic operating principles of the antenna in the last chapter, I am left with the genuine, classical control problem of finding and tracking the smoothly-varying small number of optimal input parameters to the pattern synthesis method, robustly, in real-time. In the next section, I briefly discuss the ways in which the pattern synthesis optimization approach developed in chapter 3 falls short of providing an adaptive antenna before introducing the feedback-controller that solves these problems in section 4.2.3.

4.2.2 Why pattern synthesis optimization does not an adaptive antenna make

There are two main problems in the implementation of the pattern synthesis technique demonstrated in the previous chapter that prevent the method from being used on an antenna when deployed that must be remedied to achieve an adaptive antenna according to the definition in the previous section. The first problem is the algorithm selected for optimization - the gradient-based back-tracking line search (GB-BTLS). The second problem is the inability to evaluate the objective function indicated in that work when operating in the field - the objective required measurements of specific points of the far-field pattern, which are unattainable during operation.

The GB-BTLS, obviously, required a computation of the gradient to optimize the two parameters α_1 and φ_1, and it then optimized one parameter at a time with the back-tracking line search. This approach is well-suited for limited use in a factory calibration setting where conditions are controlled and the goal is to quickly obtain the one, "best" answer for each scan angle. Additionally, this optimization in the factory will characterize the antenna at certain states to mitigate the effects of manufacturing variabilities on beam performance.

Also, when using a computational model, it is reasonable to apply two different patterns to calculate a gradient. However, during operation where each pattern takes time to apply and obtain feedback from, one does not want to sacrifice the time and possible performance in merely calculating a gradient to begin the optimization.

In addition, the GB-BTLS is highly susceptible to the measurement errors that are inevitable in a live measurement system, so a more robust controller is required. When these antennas go out into the field their behavior will continue to vary. Temperature fluctuations, atmospheric conditions, vibrations, dust, time, etc. will all cause changes in antenna response; one cannot possibly predict and factory-optimize for every condition the antenna may encounter throughout its lifetime on a plane, train, boat, or vehicle. Thus, it is necessary to have a machine-intelligent controller live on-board the antenna to continually monitor the beam and make modifications of the controls to achieve optimal performance.

The second issue preventing the pattern synthesis technique introduced in the previous chapter from being considered an adapative antenna algorithm, the objective function defined in the first work assumes that two specific points in the far-field can be monitored at all times, the main beam level and the sidelobe level. However, a measurement of the sidelobe level is not attainable from the satellite communications hub (during transmit) or directly from the signal strength (during receive) in real-time. One instead would like to consider objective functions which are measurable outside of the factory, during operation.

This chapter addresses these two problems in implementation of the pattern synthesis approach for sidelobe reduction. In this chapter, I demonstrate the use of feedback control to enable continuous optimization of the beam pattern of a RHMA. I use the pattern synthesis approach of sidelobe cancellation and leverage classical control theory to design an adaptive controller for robust feedback control of the beam pattern of the RHMA. Specifically, I implement an extremum-seeking controller (ESC) [110, 111] to continuously optimize the parameters of the sidelobe cancellation scheme. I show that the ESC is effective, robust to measurement noise, and capable of handling dynamically changing antenna conditions. I then go further to investigate the effect of the objective function on controller performance and on beam performance. I also introduce a way to speed-up the time-to-optimality that is extraordinarily robust to measurement error, which is based on the optimal control concept of value function approximation. However, first, I next describe the controller I implemented for the RHMA control problem.

4.2.3 Extremum-seeking control theory

Again, there is a vast array of controllers and control theories with the PID controller perhaps the most well known. Again, whole conferences, societies, textbooks, courses, and much more are dedicated to the field. I select an extremum-seeking controller (ESC) from among this multitude because it is a popular, general, mature adaptive control strategy. Extremum-seeking control has been applied in applications as varied as optimal formation flight [112], control of combustion instabilities [113], and photovoltaic optimization [114]. It has, in fact, even been used for beam steering, but in the context of an optical-laser communications system [115] where the control variables are phase profiles of the optical phased arrays.

The ESC sinusoidally varies a set of input variables and measures the resulting change in the output value to find and track a local maximum of an objective function [116, 117, 110]. The ESC does not depend on a model of the system dynamics since it obtains information about the gradient of the objective function, with respect to the input variables, by comparing the output to the sinusoidal perturbation signal itself. This independence from an accurate model is a big boon to the problem of the metamaterial antenna.

The ESC for the antenna system is depicted in figure 4.1. It adds a sinusoidal perturbation, $a\sin(\omega t+\beta)$, to the system's best estimate of the input variable, $\hat{\varphi}_1$ or $\hat{\alpha}_1$, obtaining $\tilde{\varphi}_1$ and $\tilde{\alpha}_1$. The perturbed estimates, $\tilde{\varphi}_1$ and $\tilde{\alpha}_1$, goes through the antenna system and a measure of the objective function is obtained in response, J. The output signal is then filtered to remove the low-frequency components, but not attenuate the frequency of the perturbation signal. Then, the filtered signal, ρ, is multiplied by the perturbation signal to demodulate the signal, obtaining ξ. The demodulated signal is then integrated into the estimate of the the optimal control to obtain an updated $\hat{\varphi}_1$ and $\hat{\alpha}_1$.

The ESC works to find the local optimum because the sign of the demodulated signal, ξ, changes depending on whether or not the estimate is above or below the true optimum. Thus, the demodulation of the perturbed signal gives the local gradient of the objective. Also, ideally the objective function is approximately quadratic such that the magnitude of ξ is large when far away from the optimum and smoothly approaches 0 moving toward the optimum. This serves to produce large changes in the estimated control $\hat{\varphi}_1$ or $\hat{\alpha}_1$ when far away from the optimum for rapid improvement in the objective and small changes when near optimal to guarantee stable convergence.

The two-variable controller simply consists of two simultaneous ESCs. However, the perturbation signals must be separable, so they can either be at the same frequency and $\pi/2$ out of phase with each other - orthogonal to each other, or they can have different frequencies. To use a single filter for both signals, I select the phase-differential method.

4.2.4 Implementing extremum-seeking control for adaptive pattern synthesis

I implement the dual-variable extremum-seeking controller to replace the original gradient-based optimization technique on a computational model of a 200 cell single-strip antenna operating at 33 GHz (the upper resonance of the cells is at 31.8 GHz and the lower resonance is at 28.2 GHz, resulting in a cell-tuning bandwidth of approximately 11%). In this chapter, I use a circuit equivalent model to compute the response of the metamaterial antenna. This model was described and demonstrated for this type of RHMA in reference [118] and in the

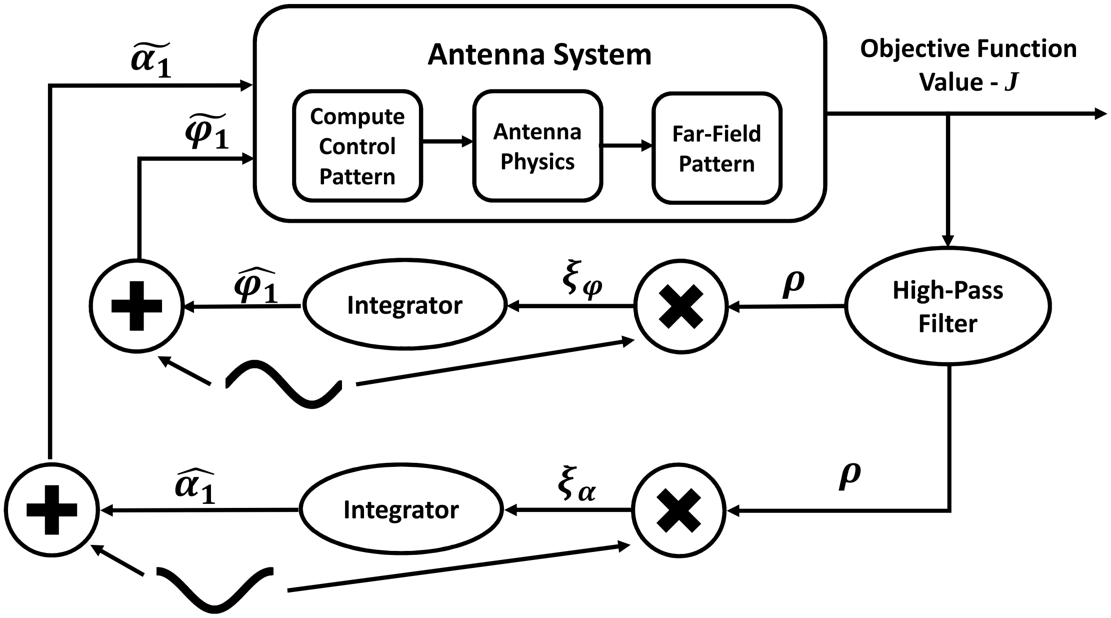

Figure 4.1: Dual-variable extremum-seeking controller for sidelobe reduction pattern synthesis on the reconfigurable holographic metamaterial antenna.

appendix A.2.

I test the use of the controller to simultaneously optimize α_1 and φ_1 for two objective functions. First, I use an objective function that is equivalent to the one used in the previous chapter that simply encourages maximal reduction the targeted sidelobe while maintaining high main beam gain:

$$J_1 = (M - S)^2, \tag{4.1}$$

where M is the main beam energy (equivalently, peak gain or directivity), in linear units, and S is the sidelobe level energy (could also be a gain or directivity value) also in linear units. The measure of the sidelobe level requires a point-based measurement that is not obtainable during operation.

Second, I demonstrate control with an objective function defined as the ratio of desired radiated energy to undesired radiated energy (D/U). I define the desired energy as the integral of the energy in the main beam and the undesired energy as the integral of the energy in the rest of the far-field pattern:

$$J_2 = \frac{\int E_{\text{main beam}}}{\int E_{\text{far-field}}} = \frac{D}{U}. \tag{4.2}$$

This objective function can be evaluated in real-time (in reality, much faster than the antenna can switch patterns) and during operation by measuring signal-strength-to-input-power or carrier-to-noise.

I implement the dual-variable ESC with the parameters shown for both objectives, $(M-S)^2$ and D/U, in table 4.1. The perturbation frequency was chosen to have enough samples per wavelength of perturbation to obtain a meaningful demodulated signal; the selected frequency works out to be 6 sample points per wavelength. The perturbation amplitudes were selected so that a change in the objective function due to the perturbation is seen, but not so large that there are large oscillations in the objective once it has obtained its optimum.

Importantly, the signal filter I use is a second-order Butterworth high-pass filter with the indicated cutoff of 0.2 in the Fourier spectrum of the digital signal (1 being the Nyquist sampling rate) at which the normalized controller gain drops to $1/\sqrt{2}$. Also, note that the only differences between the two sets of parameters for the different objectives are the controller gain values; the controller gain values need to be tuned for the absolute scale of the objective function itself.

The beam patterns resulting from the optimization can be seen in figure 4.7 for the case of a main beam designed to point at 30 degrees and the optimization algorithm targeting a sidelobe at -31.6 degrees. Note that the two objective functions results in qualitatively different reduction of the targeted sidelobe. The objective relying on point-based measurements $(M-S)^2$ reduces the targeted sidelobe about 20dB whereas the objective D/U only reduces this sidelobe by about 10dB. However, the objective D/U also reduces the sidelobe at -19 degrees whereas the $(M-S)^2$ objective significantly raises this sidelobe. That is, the objective D/U, which takes all sidelobe energy in aggregate, reduces the targeted sidelobe only to the point where the rest of the pattern starts degrading so far as to offset the improvements

Table 4.1: Dual-variable ESC parameters for RHMA pattern synthesis

	Objective $(M-S)^2$		Objective D/U	
	α_1	φ_1	α_1	φ_1
Perturb Freq, ω	$\pi/3$	$\pi/3$	$\pi/3$	$\pi/3$
Perturb Amp, a	$1e-3$	1.0°	$1e-3$	1.0°
Perturb Phase-offset, β	$\pi/2$	0	$\pi/2$	0
Cut-off Freq	0.2	0.2	0.2	0.2
Gain	1.55	900	0.05	33

made by reducing the targeted lobe.

The resulting number of function evaluations to achieve optimal answers are shown in figures 4.3 and 4.4 for the two different objectives. In the case of the objective function $(M-S)^2$, the GB-BTLS took approximately 1300 function evaluations to converge upon the optimal answer while the ESC was able to stably converge in approximately 1200 function evaluations. However, for changing environmental conditions, the GB-BTLS optimization would need to be re-initialized, whereas the ESC will adaptively vary array parameters on-line to compensate and maintain performance. For the objective function D/U, the GB-BTLS only took about 500 function evaluations, and the ESC was able to stably converge in slightly fewer, approximately 425, function evaluations. Both of these results demonstrate the ESC's ability to directly replace the gradient search efficiently, slightly reducing the number of function evaluations required to achieve optimality.

The results of the convergence of the ESC in both figures 4.3 and 4.4 have some interesting characteristics of note. Most obviously, the controller (and the gradient approach) converge much more quickly for the objective D/U than for the objective $(M-S)^2$ – almost 1/3 of the iterations are required to achieve optimality. It was impossible to raise the controller gain to try to more quickly obtain the optimum and remain stable in the case of $(M-S)^2$. Also, note the significant oscillation in the objective function value as the optimum is obtained in

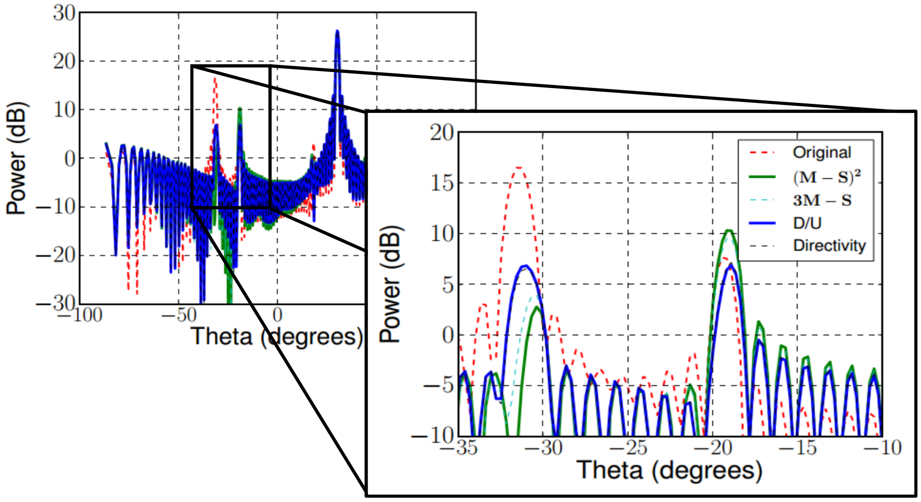

Figure 4.2: Comparison of beam patterns resulting from optimization with different objective functions. The original, unoptimized beam pattern is shown in red dashes. The point-based objectives, $J_1 = (M - S)^2$ and $3M - S$, reduce the targeted sidelobe at -32 degrees by more than 15 dB while the objective functions $J_2 = D/U$ and Directivity reduce the target lobe by only 10 dB. However, the J_2 and Directivity objectives reduce the lobe at -19 degrees, as well, while the point-based objectives actually increase this sidelobe.

the case of the $(M - S)^2$ objective, which is not seen in the D/U objective. Both of these observations indicate that the topology of the objective function D/U is much closer to the quadratic objective function that is ideal for the ESC than that of $(M - S)^2$.

These indicators of differences in the topology of the objective functions in parameter space induce me to look more closely at these functions and consider other functions, as well, which could provide different and more favorable convergence behaviors. This I do in section 4.3.

4.2.5 Problems solved with feedback control

The aim in replacing the gradient-based optimization with an adaptive controller was to introduce a mechanism for live, continuous optimization of the beam pattern. There are several issues that the antenna experiences when outside of the controlled manufacturing environment for which the antenna needs to be able to automatically adjust itself. These

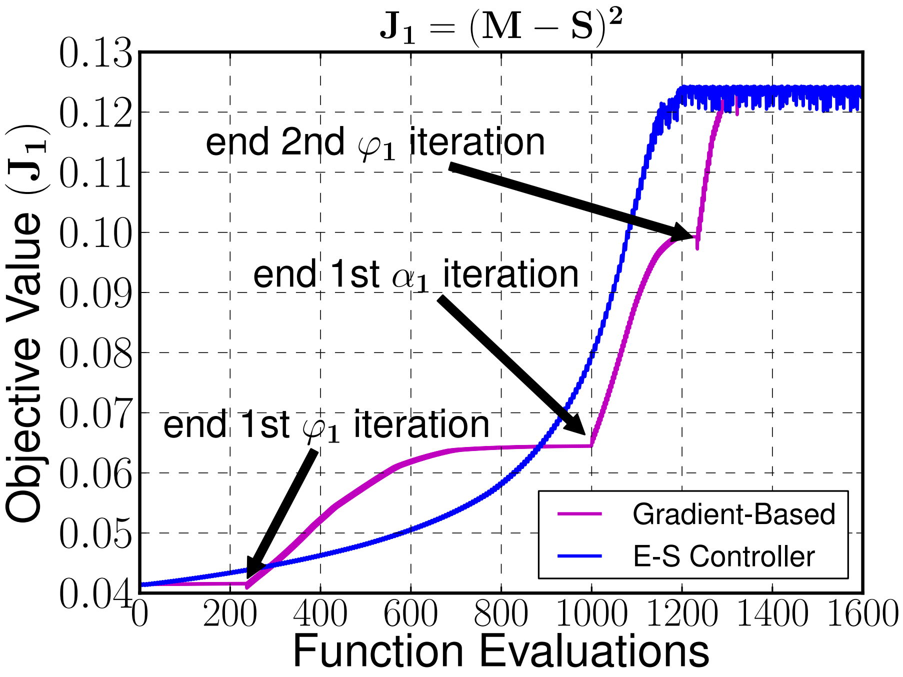

Figure 4.3: Comparison of the number of function evaluations required to obtain the optimal solution for the gradient-based optimization with back-tracking line search and the extremum-seeking controller for the objective function $J_1 = (M - S)^2$.

external factors cannot always be predicted, so that they cannot be handled adequately by open-loop or disturbance-feedforward control.

Measurement error rejection

Measurement error will always be present during operations. The GB-BTLS is susceptible to measurement error, as one wrong estimate of the gradient will send the algorithm in the wrong direction and prematurely stall the optimization. On the other hand, the ESC takes several samples per perturbation wavelength and integrates the filtered and demodulated signal, providing a robustness to measurement noise. In figure 4.5, I demonstrate the behavior of the two optimizations in the presence of measurement error. I model the measurement error as Gaussian white noise process ($\mu = 0$) with increasing variance. The GB-BTLS fails to find

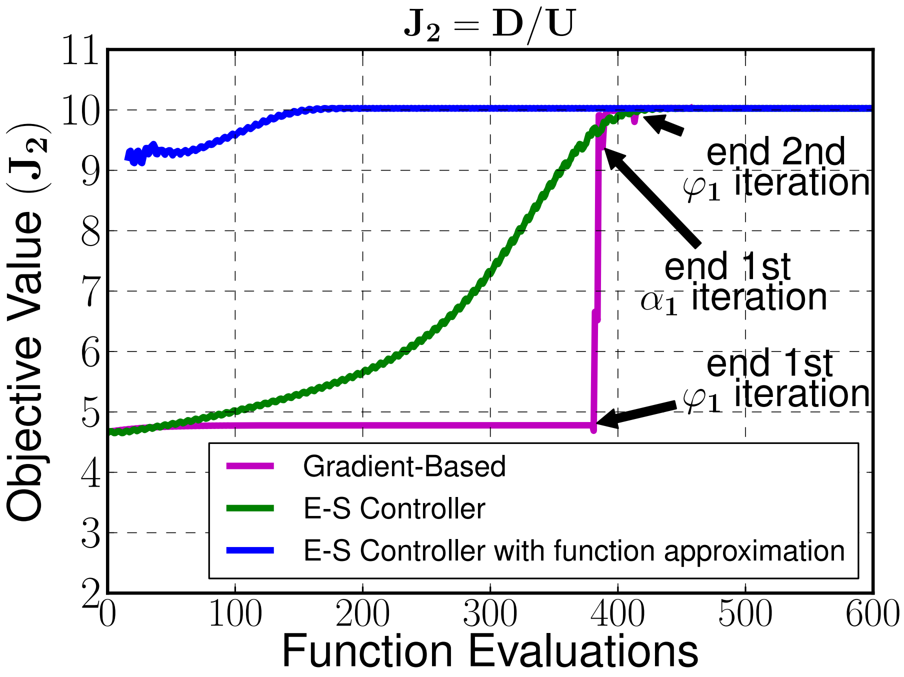

Figure 4.4: Comparison of the number of function evaluations required to obtain the optimal pattern for the gradient-based optimization with back-tracking line search, the extremum-seeking controller from the same uninformed initialization, and the extremum-seeking controller initialized with the best-estimate from function approximation for the objective function $J_2 = D/U$. The improved initialization from function approximation reduced the number of required evaluations by more than half.

the correct solution at all non-zero noise levels. The ESC, on the other hand, is robust to all levels of noise, though for the three larger values of σ the controller gain must be reduced for both variables to maintain stability. It takes longer to arrive at the optimal solution, but the controller successfully converges to the correct solution where the GB-BTLS fails.

Antenna behavior change mitigation

Another reason to use feedback control is to compensate for changes in the behavior of the antenna over time. These changes may be in response to temperature, atmospheric conditions, rain, dust, or materials degradation. Perhaps the most easily interpreted of these situations of slowly-varying antenna conditions is the antenna behavior with temperature. The unit-cells modeled in this work display resonant frequency variation with changing temperature, for both the on and off states. Both frequencies shift downward from the nominal resonance locations at cooler temperatures (below approx 70 degrees Fahrenheit) and shift upward at warmer temperatures. These shifts, though less than +/-250 MHz when going from 5 to 80 degrees C, are enough to affect the response of the cells and the resulting beam pattern.

I demonstrate a simple case in which the antenna is warming up from a cold start in figure 4.6. The controller begins at time (function evaluation) 0 with the optimal controls at the cold temperature, where the resonant frequencies of the cells are 250MHz below the nominal resonance. As the antenna is running, the temperature begins increasing, so the resonant frequencies of the cells shift upward. The ESC-based controller is able to continue to stably find and track the optimal parameter values despite the fact that the optimal value and optimal parameters are varying as the antenna response is continuously changing. The controller allows for continued high-performance whereas continuing to use the optimal parameters established at the lower temperatures results in performance degradation.

4.3 Objective Functions

Returning to the interesting characteristics seen in the controller results of section 4.2.4, I visualize the objective functions $(M-S)^2$ and D/U. I also look at two more functions that are similar in the beam pattern they elicit, but that may have more favorable geometry. Similar to the objective $(M-S)^2$, I try a linearly weighted version, which should not be as peaked around the optimal point and that penalizes peak beam gain loss more heavily, $J = 3M - S$. And similar to the aggregated pattern effect of the objective D/U, I also try an objective function given by the peak directivity.

The three-dimensional surfaces, as well as their contour projections on the $J = 0$ plane, for all four functions are shown in figure 4.7. The functions that depend on an integrated value are somewhat smoother in parametric space than the functions with point-based measurements. However, the more detailed view in figure 4.8 gives a better understanding of the oscillations observed in figures 4.3 and 4.4 at the peak of the $(M-S)^2$ and D/U objectives. The objective $(M-S)^2$ has a fairly constant gradient until near the optimum, and then there is a plateau-like region. Thus, the gradient does not smoothly approach zero as one approaches the optimum, which causes larger oscillations and greater instability of the ESC.

On each surface plot, I have also plotted the trajectory of the two ESC controllers whose results were shown in figures 4.3 and 4.4. The ending, optimal point of the controller of the $(M-S)^2$ objective (the blue dot) overshoots the peak of the directivity and D/U objectives, while the ending point of the controller of the D/U objective is significantly sub-optimal in the $(M-S)^2$ objective. It is also seen, as expected, that the peak of the two point-based objectives are close in parameter space, while the peaks of both of the aggregate objectives are nearly coincident as well. It is important, also, to examine the resulting beam patterns induced by each objective. This is shown in figure 4.2. The objectives that include an integrated value do not reduce the targeted sidelobe as much, as noted previously, since the noise floor of the pattern begins creeping up such that the benefit from further sidelobe reduction does not out-weigh the degradation of the rest of the pattern.

It is evident that the definition of the objective function is an important consideration when attempting to achieve the desired performance goal. Also, the behavior of the objective function has an effect on the controller's convergence rate and stability. I have only extensively considered the two objectives demonstrated in the previous section, and I have chosen to move forward with the D/U objective since it is attainable during operation and displays superior convergence behavior and stability. Yet, many other objective functions could be pursued with this approach including null-steering for adjacent satellite interference mitigation and perhaps even more exotic beam-tailoring like multiple beams for continuous connection during hand-off.

4.4 Combining Function Approximation

In section 4.2.4 I demonstrated the dual-variable ESC for on-line optimization through feedback control, and in section 4.3 I looked at a variety of objective functions. Yet, one would like to further reduce the number of function evaluations required to reach optimality as each pattern applied to the antenna takes time, perhaps jeopardizing real-time optimization. If one initializes the controller from a position in parameter space nearer the optimum, one can achieve the peak with many fewer control patterns tested. There are several ways one can envision obtaining a good initialization. One way to initialize the controller close to optimum would be to do hundreds of thousands of tests on hardware under many of the conditions that the antenna might encounter and learn, from the data, appropriate initial conditions. This is akin to a library learning task used commonly in machine learning strategies [119]. This method is obviously prohibitive from the amount of testing that would be required. Otherwise, one could possibly use the exact analytic answer that could be obtained assuming the antenna physics are completely linear and the antenna is perfectly made to reflect the designed aperture. The problem here is that the assumptions begin to take one quite far from the realizable hardware, and thus the initialization point degrades, as well. One could also use the original gradient-based optimization to do a detailed factory calibration/optimization. These factory calibrations will be important, but they are insufficient in that all the situations likely to be encountered by the antenna cannot possibly be anticipated and prepared for in the factory setting.

I propose, instead, a much different approach to finding a good initial condition. In my approach, an approximation to the objective function is obtained from a few sample points throughout the parameter space. I then initialize the controller from the optimal point of the approximate function. This approach is based on value function approximation techniques which have been attempted, largely unsuccessfully to date, to improve the computational efficiency of trajectory optimizers [120, 121, 86, 122].

I believe that function approximation will be much more viable here for two reasons.

First, the parameter space is small and is well-behaved, particularly in comparison to the complex geometries of the objectives and unstable dynamics in the systems for which trajectory optimizers are seeking to make optimal control possible (e.g. robot walking, dextrous manipulation, etc.). Second, when using value function approximation in trajectory optimization, one needs an accurate approximation of the function at every control state on and near the likely states throughout the entirety of the parameter space. my problem is considerably simpler because all that is needed from the approximation is a good indication of the location of the peak of the function.

I try value function approximation for the objective function of D/U, which appears to be a nearly quadratic function. Thus, I create a least-squares best-fit quadratic surface approximation to several sampled points in the parameter space. An example of the best-fit quadratic surface when 16 equally spaced points between -0.5 and -0.35 in α_1 and -90 and $+90$ in φ_1 are used for samples is shown in figure 4.9. This approximate function can be compared with the true surface in figure 4.7; the approximation does not have the ridge that is visible in the true surface, but, again, my aim is just to obtain a good starting point close to the optimal parameters. The critical point of the approximated function is simply obtained by differentiation of the polynomial surface. The peak of the demonstrated approximated function is shown as a diamond in figure 4.9 while the location of the true peak is indicated by a triangle. I run the ESC with initialization from the approximate value function and compare the number of function evaluations necessary to achieve the optimal controls to the ESC without the informed initialization, which was demonstrated in section 4.2.4. The result is also shown in figure 4.4 of that earlier section for ease of comparison with the uninformed initialization. The improved initialization reduces the number of required function evaluations by about half, in this case.

The robustness of the proposed initialization process under noise is again of paramount importance. I take so few sample points from the parameter space to create the approximation that significant error in one or all of them could heavily skew the resulting approximation. To test the robustness, I inject noise into the sample points, before constructing the function approximation, as done previously in section 4.2.5. I do this for 100 trials at each noise level. The results shown in figure 4.10 indicate that injecting noise does not greatly degrade the approximation, and still provides benefit over doing nothing. This result is very encouraging as it indicates that the approach will be extremely robust to the invariable errors produced during operation in a noisy real-world environment.

Summary

In this chapter, I took the final step toward a self-optimizing metamaterial antenna by introducing continuously adaptive beam pattern control for the RHMA. First, I implemented an extremum-seeking controller to achieve adaptive pattern synthesis that is robust to noise and capable of finding and tracking the optimal control parameters as the behavior of the antenna changes. For example, I demonstrated robust performance as a change in temperature caused the response of the unit cells to also change.

Second, I explored different objective functions. The controller was able to optimize the parameters for both objectives J_1 and J_2, yet these two different objectives yielded different resulting beam patterns. The objective $J_2 = D/U$ was smoother, yielding better convergence with the controller, and has the important property that it can be measured during operation. Yet, it is worth note, that many other objective functions might be used with the same control approach to achieve other goals like interference mitigation.

Finally, I also effectively used value function approximation to expedite the convergence of the ESC. I demonstrated that fitting a quadratic function to only a few sample points can be used to provide an excellent initialization to the controller. I also found that this method was extremely robust to noise in the measurement of the sample points. This technique allows the antenna to rapidly, at any scan angle or operating condition (not just the ones tested or calibrated in the factory), find an excellent approximation of the optimal parameters with which to initialize the controller. This work, following on the pattern synthesis approach presented in the previous chapter, represents a significant step toward robust, adaptive control of the beam pattern of a reconfigurable holographic metamaterial antenna. It is the first work to demonstrate a complete closed-loop feedback control methodology for dynamic optimal pattern synthesis of the RHMA, thus enabling a practical, smart, software architecture for such antennas.

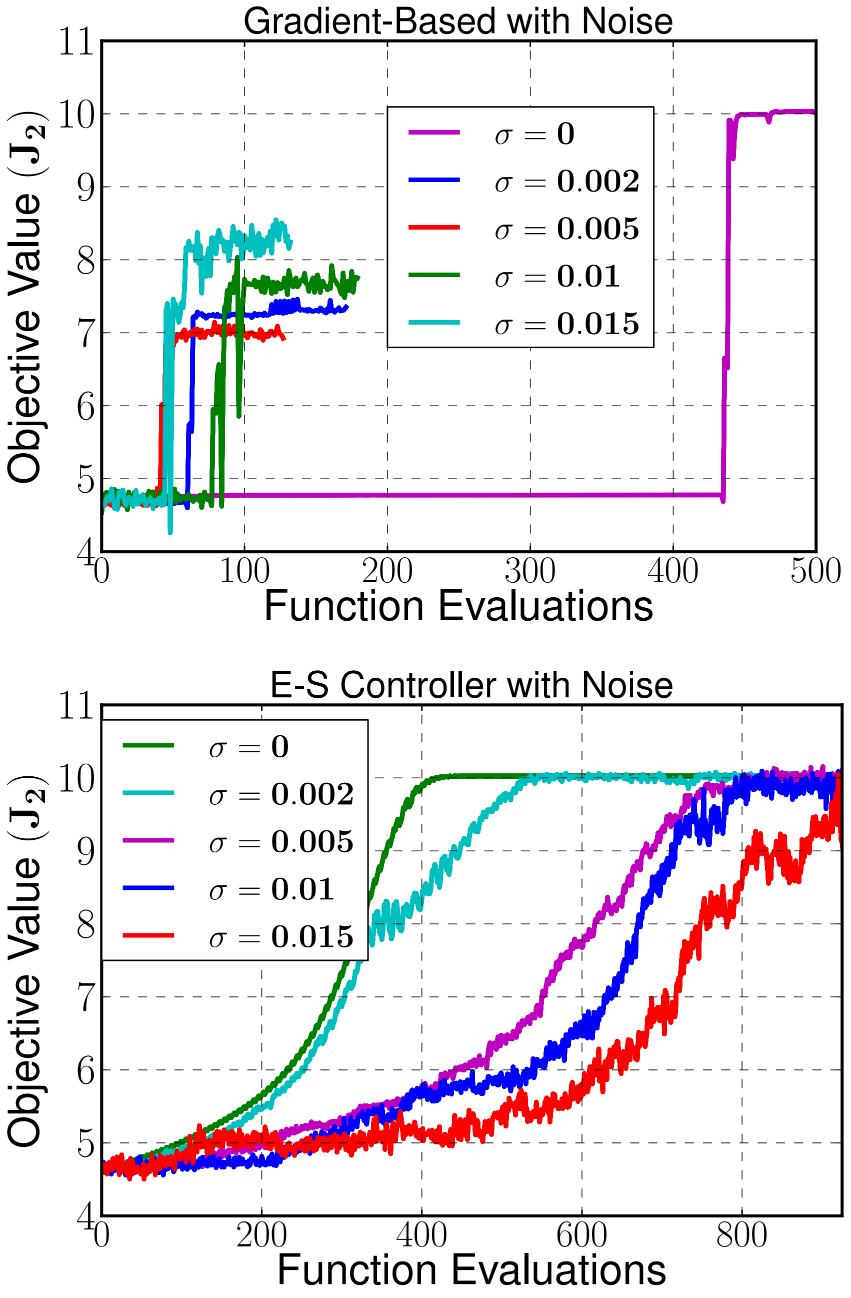

Figure 4.5: Convergence of gradient-based optimization (top) and extremum-seeking control (bottom) in the presence of Gaussian measurement noise with increasing standard deviation, σ. The gradient-based optimization fails to converge to the optimal answer for any level of measurement noise whereas the extremum-seeking control is robust to all levels of noise.

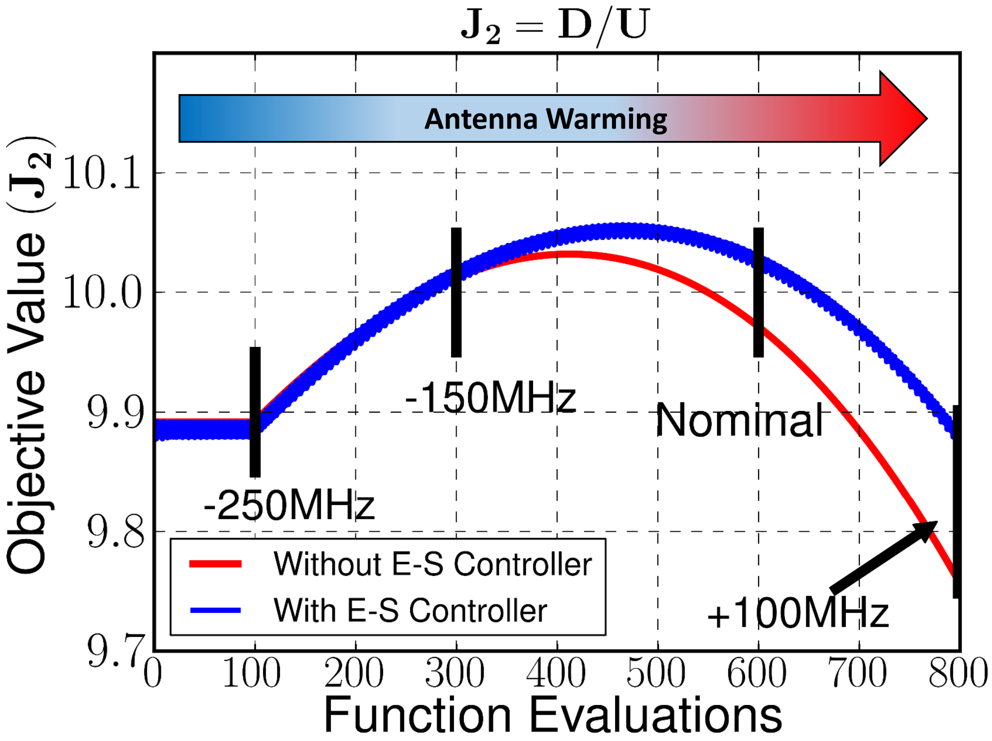

Figure 4.6: Example of extremum-seeking controller performance when the antenna is warming up, affecting the resonant frequencies of the cells. The antenna begins at the optimal performance for the cooler temperature. As the temperature rises, the controller stably maintains the optimum though the optimal value and optimal parameters are changing as a result of the change of the response of the antenna, providing improved performance over simply using a static one-temperature-optimal solution.

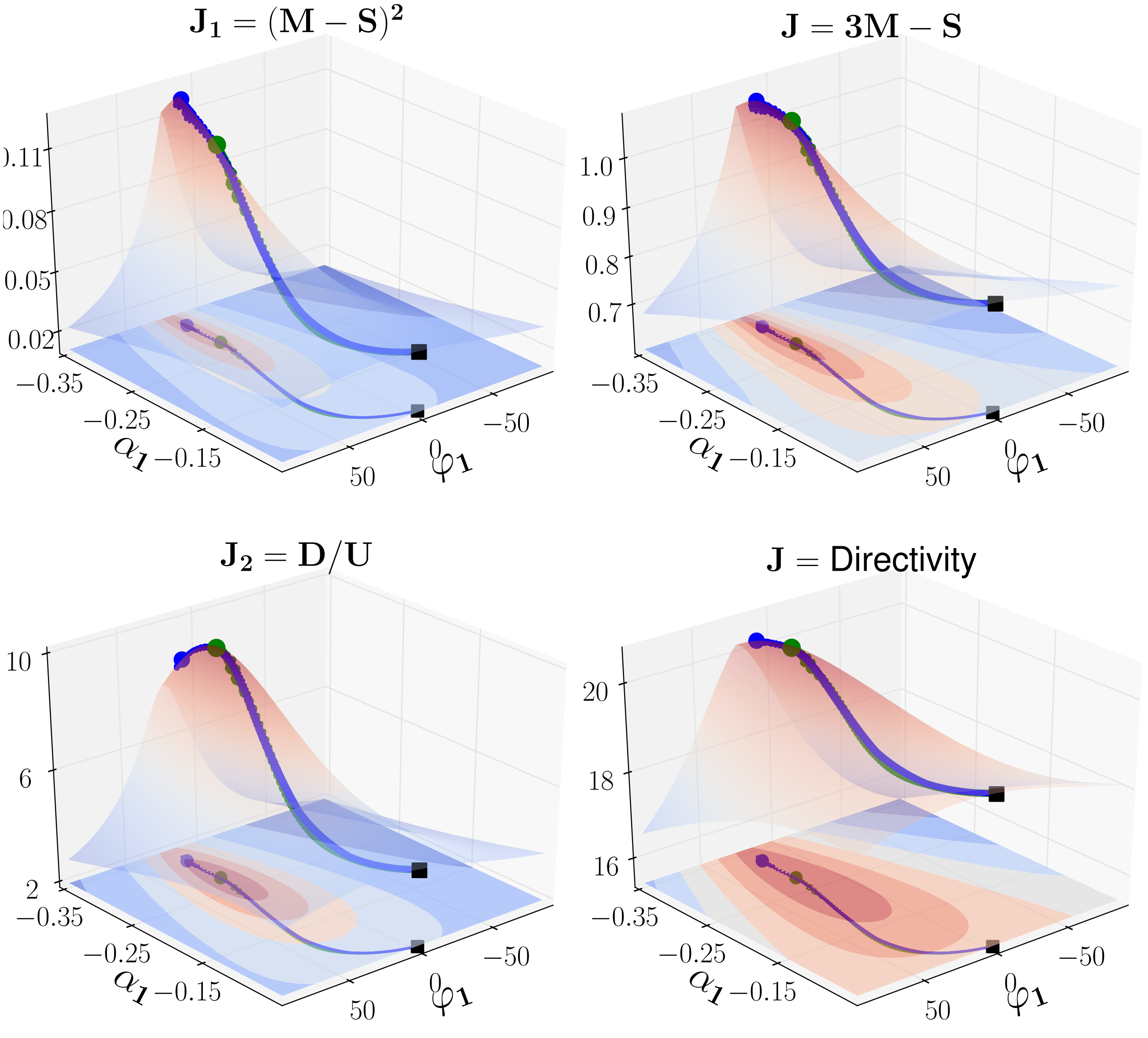

Figure 4.7: Three-dimensional depictions of several objective functions in parameter space, α_1, the parametric, unit-free weighting variable, and φ_1, the phase-shift variable shown in degrees. (Clockwise from top left) $J_1 = (M - S)^2$, $(M - S)$, Directivity, $J_2 = D/U$. The blue trace on the surfaces correspond to the trajectories of the extremum-seeking controller seeking an optimum in the objective $J_1 = (M - S)^2$, as seen in the blue curve in figure 4.3. The green trace, which is less visible because it includes many fewer iterations, corresponds to the trajectories of the extremum seeking controller seeking an optimum in the objective $J_2 = D/U$, which is seen in the green curve of figure 4.4.

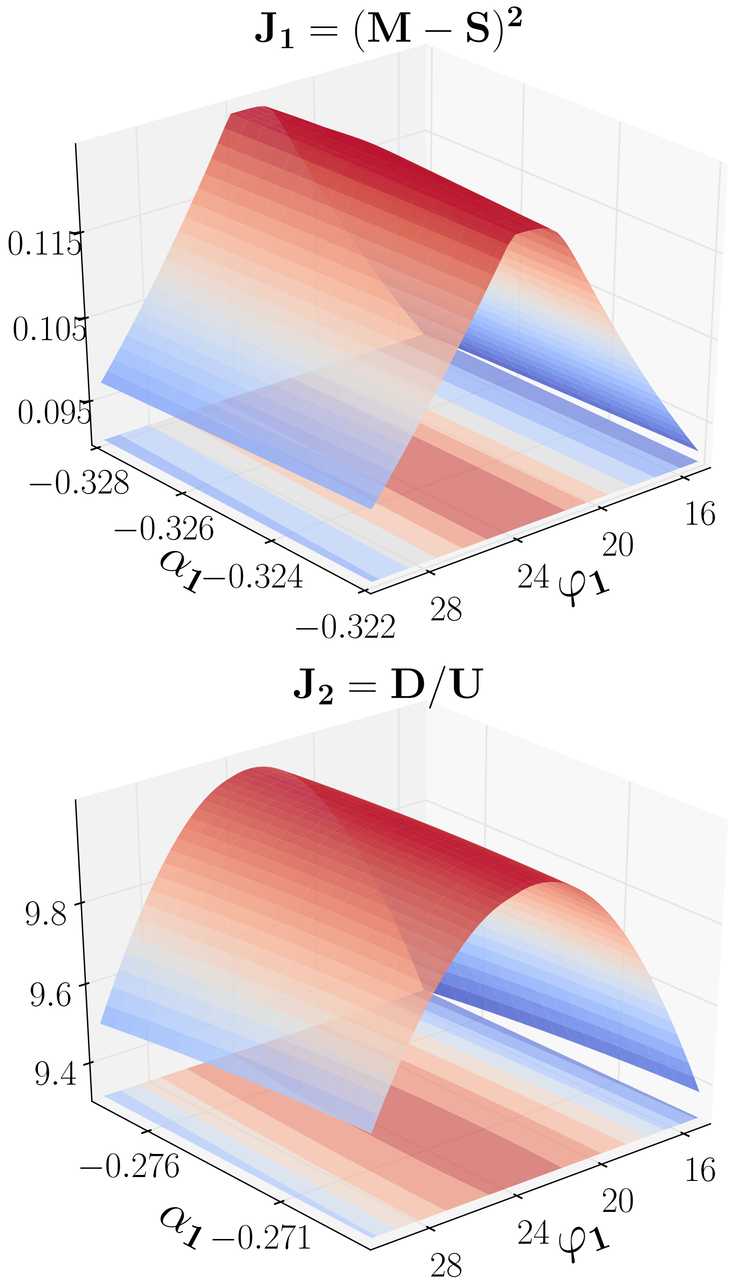

Figure 4.8: Behavior of objectives J_1 and J_2 near their optimal values as a function of the two optimization parameters α_1, the unit-less weighting variable, and φ_1, the phase-shift variable shown in degrees. Note that the magnitude of the gradient in the case of J_1 does not diminish as it approaches the optimal. Rather, the gradient is large, and then turns a corner to become nearly zero. The objective J_2 has smooth, locally-quadratic behavior improving the stability of the convergence of the extremum-seeking controller.

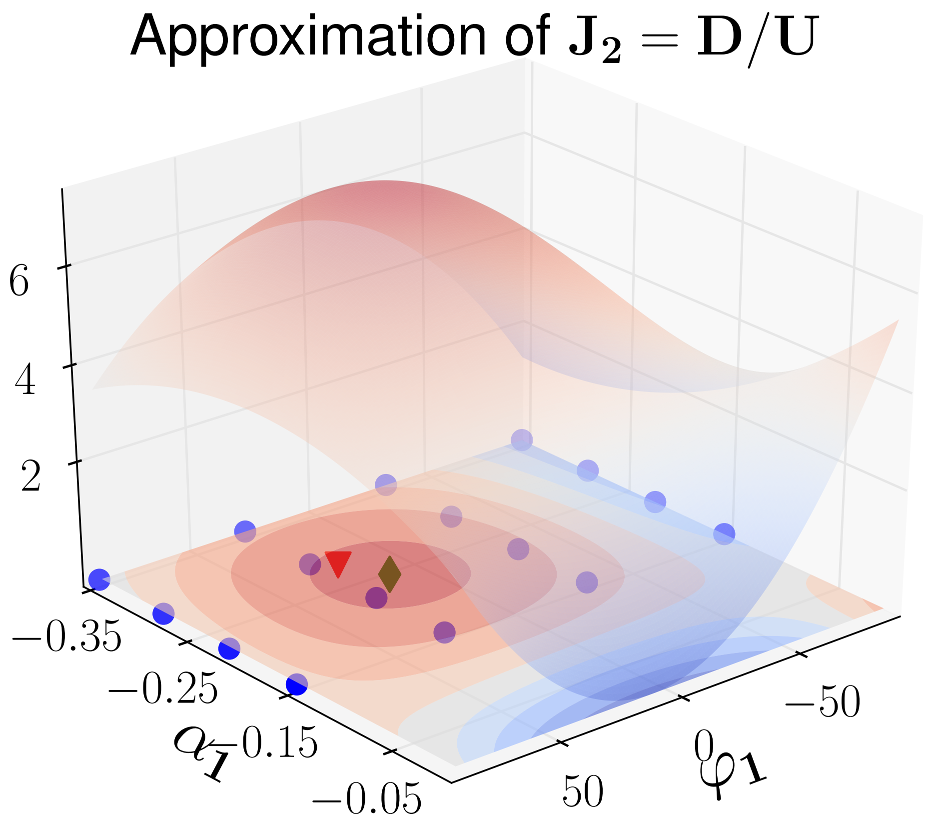

Figure 4.9: Three-dimensional depiction of the approximation of objective J_2. The green diamond indicates the optimal parameters as estimated by the approximate function while the red triangle shows the optimal parameters of the exact objective function. The blue dots indicate the sample points where the true function (see figure 4.7) was evaluated to obtain the approximate surface shown here.

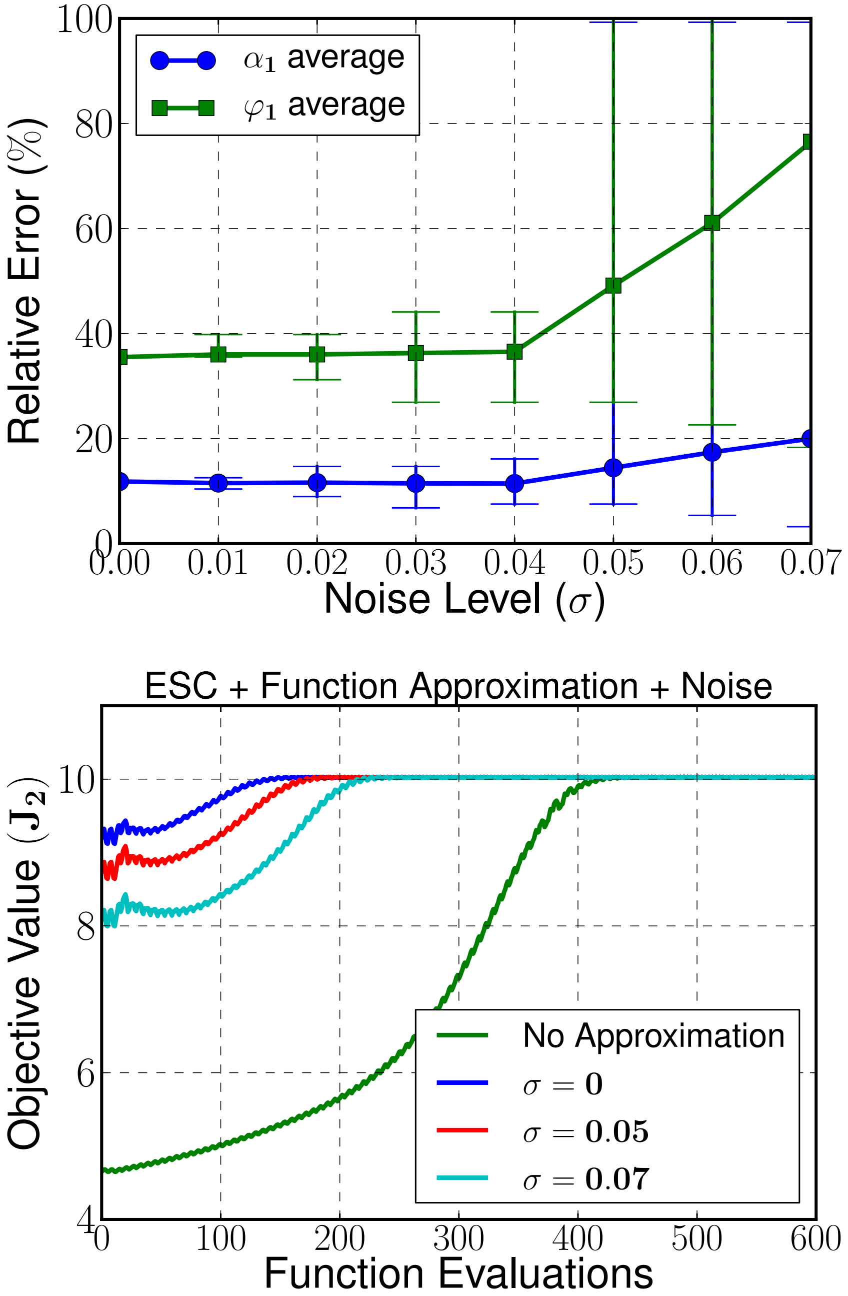

Figure 4.10: (Top) Percentage relative error in the estimated optimal parameters for 100 trials at each noise level. The larger markers indicate the average while the lines show the minumum and maximum errors over all trials. (Bottom) Extremum-seeking controller trajectories resulting from initializing the controller with the average value from all 100 runs at each noise level.

Chapter 5

CONCLUSIONS AND FUTURE WORK

This thesis has developed one route toward adaptive, self-optimizing metamaterial antennas. I developed a pattern synthesis technique particular to the holographic antenna, and I demonstrated how this pattern synthesis technique can be used adaptively, continuously during operation via an extremum-seeking feedback controller.

In chapter 2, I laid the groundwork and built the platform that enabled testing of software-based pattern synthesis for the RHMA. This was a model of the antenna physics based on the Discrete Dipole Approximation. I demonstrated that this model was more accurate than simpler models. I also achieved the other purpose in pursuing light-weight, semi-analytic modeling of the antenna that was to have a fast computational model. This model gave both an accurate means of studying the characteristic patterns of the RHMA and an efficient means of exploring and designing pattern synthesis techniques to improve these characteristic patterns.

In the next chapter, I introduced the topic of pattern synthesis for electronically-steered antennas, and this thesis's contribution was to design a synthesis technique that effectively exploited the RHMA's holographic principles to reduce undesired sidelobes. This chapter explored pattern synthesis for the RHMA from the phased array and holographic perspectives, both yielding useful insight into the production of sidelobes and, thus, the means of removing them. Then, I stepped beyond the traditional pattern approach to eliminate targeted sidelobes by engineering of the control patterns. I demonstrated both in simulation and in experiment that the technique is effective, and thus, gives a principled means of improving the RHMA radiation pattern on a manufactured device.

Finally, in chapter 4, I took the last step toward an adaptive RHMA, which was to introduce a feedback controller to synthesize optimal, reduced-sidelobe patterns live on an antenna. I demonstrated that an extremum-seeking controller combined with the newly-developed pattern synthesis approach is able to handle significant measurement error, which is always present during operation. In addition, I showed one example in which the controller handles a varying environment. These computational examples are an indication of what is needed for machine-intelligent, flexible pattern control of a metamaterial antenna, and they also demonstrate the promise of a feedback control approach combined with a pattern synthesis technique specific to an RHMA to solve the problem of robust, continuous antenna control. In this chapter, I also successfully integrated an additional layer to the feedback controller, objective function approximation. This technique allows the antenna to rapidly, at any scan angle or operating condition (not just the ones tested or calibrated in the factory), find an excellent approximation of the optimal parameters with which to initialize the controller. This work is the first work to demonstrate a complete closed-loop feedback control methodology for dynamic optimal pattern synthesis of the RHMA, thus enabling an intelligent software architecture for such antennas.

Altogether, this thesis has moved the reconfigurable, holographic metamaterial antenna from a unique, complex, and promising piece of hardware engineering achievement to a smart, unique, complex, and promising piece of hardware and software engineering. The size, weight, and low-power consumption of the RHMA gives it a significant advantage over gimballed reflectors, and the low-cost gives it an advantage over phased arrays. Yet, these physical characteristics must be combined with the functionality of the smart, adaptive, software-driven beam steering of the metamaterial antenna in order to revolutionize the mobile satellite communications technology industry.

As such, it is important that this work in adaptive software-based control for the RHMA continue to be pursued. I have just made a first foray into robust, machine-intelligent control of the metamaterial antenna. i developed one pattern synthesis technique and one adaptive controller that is compatible with this technique. Yet, there are several burgeoning fields of study that can be leveraged to develop still more capable and flexible controllers. These methods include all the most popular topics of the applied mathematical community today including machine learning, data-driven modeling, dimension reduction, compressive sensing and convex optimization, and uncertainty quantification.

For one, machine learning approaches and data-driven modeling can be used to better characterize and understand the antenna purely from data. These methods are designed to automatically find structure within the complex input-output response of the system (reducing the dimension of the system) [123]. They can identify characteristic behaviors in various regimes of operation that might otherwise be hidden. These improvements in understanding can be leveraged to better design and analyze advanced analytic models, and they can also be used directly with compatible control methods - the machine learning identifying the antenna state and then the appropriate control algorithm being applied. Further, one can leverage the information gained in dimension reduction through machine learning with compressive sensing.

Compressive sensing is a mathematically rigorous framework that tractably makes it possible to recover a complex signal, image, or state from a minimal set of measurements if the the complex signal, image, or state has an underlying low-dimensional nature [124]. In this way, with the knowledge of the structure of the data gained in machine learning, compressive sensing provides the means by which control decisions can be made quickly - with as few measurements or trials as possible.

Uncertainty quantification (UQ) is one more blooming area of research that might provide advancement for the control capabilities of the metamaterial antenna [125]. The entire field of UQ is dedicated to developing means to understand and govern complex systems that are difficult or impossible to observe fully. UQ would provide insight into the design and, importantly, the control variables that are most significant to optimality of the antenna's radiation pattern. Initially, UQ could prove beneficial in identifying control patterns or techniques that are more robust to variations across the array due to manufacturing processes, providing increased bandwidth and continuously stable high-performance.

The future of the metamaterial antenna as a wide-spread consumer technology rests on its software capabilities, and the future possibilities of those software capabilities is bright; there are many promising avenues for creating smart RHMA algorithms. This thesis developed and demonstrated one such adaptive control approach for the RHMA, the first to be derived for and proven on an RHMA.

BIBLIOGRAPHY

[1] Richard A. Shelby, David R. Smith, and Seldon Schultz. Experimental verification of a negative index of refraction. *Science*, 292(5514):77–79, 2001.

[2] David Schurig, J.J. Mock, B.J. Justice, Steven A. Cummer, John B. Pendry, A.F. Starr, and David R. Smith. Metamaterial electromagnetic cloak at microwave frequencies. *Science*, 314(5801):977–980, 2006.

[3] Guy Lipworth, Alex Mrozack, John Hunt, Daniel L. Marks, Tom Driscoll, David Brady, and David R. Smith. Metamaterial apertures for coherent computational imaging on the physical layer. *Journal of the Optical Society of America A*, 30:1603–1612, 2013.

[4] Matthias Wuttig and Noboru Yamada. Phase-change materials for rewriteable data storage. *Nature materials*, 6(11):824–832, 2007.

[5] Sébastien Guenneau, Alexander Movchan, Gunnar Pétursson, and S. Anantha Ramakrishna. Acoustic metamaterials for sound focusing and confinement. *New Journal of physics*, 9(11):399, 2007.

[6] Jeffrey B. Chou, Yi Xiang Yeng, Yoonkyung E. Lee, Andrej Lenert, Veronika Rinnerbauer, Ivan Celanovic, Marin Soljačić, Nicholas X. Fang, Evelyn N. Wang, and Sang-Gook Kim. Enabling ideal selective solar absorption with 2d metallic dielectric photonic crystals. *Advanced Materials*, 2014.

[7] B.D. Bala, M.K.A. Rahim, and N.A. Murad. Composite right/left-handed dual-band metamaterial antenna with improved gain and efficiency. *Microwave and Optical Technology Letters*, 56(7):1575–1579, 2014.

[8] Andrea Alù, Filiberto Bilotti, Nader Engheta, and Lucio Vegni. Subwavelength, compact, resonant patch antennas loaded with metamaterials. *Antennas and Propagation, IEEE Transactions on*, 55(1):13–25, 2007.

[9] Te-Kao Wu. *Frequency Selective Surfaces*. Wiley Online Library, 1995.

[10] Q. Wu, P. Pan, F.Y. Meng, L.W. Li, and J. Wu. A novel flat lens horn antenna designed based on zero refraction principle of metamaterials. *Applied Physics A*, 87(2):151–156, 2007.

[11] Arthur C Clarke. Extraterrestrial relays. *Wireless world*, 51(10):305–308, 1945.

[12] KARL Ferdinand Braun. Electrical oscillations and wireless telegraphy. *Nobel Lecture, December*, 11(1909):226–245, 1909.

[13] Takashi Iida and Joseph N. Pelton. Satellite antenna systems design and implementation around the world. In *Handbook of Satellite Applications*, pages 397–426. Springer, 2013.

[14] Christophe Caloz and Andreas Rennings. Overview of resonant metamaterial antennas. *EuCAP 2009*, 2009.

[15] Sergei Alexander Schelkunoff and Harald T. Friis. *Antennas: theory and practice*, volume 639. Wiley New York, 1952.

[16] Victor Georgievich Veselago. The electrodynamics of substances with simultaneously negative values of ϵ and μ. *Physics-Uspekhi*, 10(4):509–514, 1968.

[17] David R. Smith and Norman Kroll. Negative refractive index in left-handed materials. *Physical Review Letters*, 85(14):2933, 2000.

[18] Nader Engheta and Richard W. Ziolkowski. *Metamaterials: physics and engineering explorations*. John Wiley & Sons, 2006.

[19] Wenshan Cai and Vladimir M. Shalaev. *Optical metamaterials*, volume 10. Springer, 2010.

[20] Tie Jun Cui, David R. Smith, and Ruopeng Liu. *Metamaterials: theory, design, and applications*. Springer, 2009.

[21] Christophe Caloz and Tatsuo Itoh. *Electromagnetic metamaterials: transmission line theory and microwave applications*. John Wiley & Sons, 2005.

[22] John B. Pendry. Metamaterials: Transformation optics. *New Scientist*, 209(2794):iv–v, 2011.

[23] Nathan Kundtz, Daniel Gaultney, and David R. Smith. Scattering cross-section of a transformation optics-based metamaterial cloak. *New Journal of Physics*, 12(4):043039, 2010.

[24] John B. Pendry, A.J. Holden, D.J. Robbins, and W.J. Stewart. Magnetism from conductors and enhanced nonlinear phenomena. *Microwave Theory and Techniques, IEEE Transactions on*, 47(11):2075–2084, 1999.

[25] Victor V. Gozhenko, Anthony K. Amert, and Keith W. Whites. Homogenization of periodic metamaterials by field averaging over unit cell boundaries: use and limitations. *New Journal of Physics*, 15(4):043030, 2013.

[26] H. Liu, D.A. Genov, D.M. Wu, Y.M. Liu, J.M. Steele, C. Sun, S.N. Zhu, and X. Zhang. Magnetic plasmon propagation along a chain of connected subwavelength resonators at infrared frequencies. *Physical review letters*, 97(24):243902, 2006.

[27] H. Liu, Y.M. Liu, T. Li, S.M. Wang, S.N. Zhu, and X. Zhang. Coupled magnetic plasmons in metamaterials. *physica status solidi (b)*, 246(7):1397–1406, 2009.

[28] Mingkai Liu, David A. Powell, Ilya V. Shadrivov, and Yuri S. Kivshar. Optical activity and coupling in twisted dimer meta-atoms. *Applied Physics Letters*, 100(11):111114–111114, 2012.

[29] Joerg Petschulat, C Menzel, A. Chipouline, Carsten Rockstuhl, A. Tünnermann, F. Lederer, and T. Pertsch. Multipole approach to metamaterials. *Physical Review A*, 78(4):043811, 2008.

[30] Ricardo Marqués, Francisco Mesa, Jesus Martel, and Francisco Medina. Comparative analysis of edge-and broadside-coupled split ring resonators for metamaterial design-theory and experiments. *Antennas and Propagation, IEEE Transactions on*, 51(10):2572–2581, 2003.

[31] Patrick T. Bowen, Tom Driscoll, Nathan B. Kundtz, and David R. Smith. Using a discrete dipole approximation to predict complete scattering of complicated metamaterials. *New Journal of Physics*, 14(3):033038, 2012.

[32] Sergei A. Tretyakov and Ari J. Viitanen. Plane waves in regular arrays of dipole scatterers and effective-medium modeling. *JOSA A*, 17(10):1791–1797, 2000.

[33] Sungjoon Lim, Christophe Caloz, and Tatsuo Itoh. Metamaterial-based electronically controlled transmission-line structure as a novel leaky-wave antenna with tunable radiation angle and beamwidth. *Microwave Theory and Techniques, IEEE Transactions on*, 52(12):2678–2690, 2004.

[34] Christoph Menzel, Thomas Paul, Carsten Rockstuhl, Thomas Pertsch, Sergei Tretyakov, and Falk Lederer. Validity of effective material parameters for optical fishnet metamaterials. *Physical Review B*, 81(3):035320, 2010.

[35] M. Lapine and Sergei A. Tretyakov. Contemporary notes on metamaterials. *Microwaves, Antennas & Propagation, IET*, 1(1):3–11, 2007.

[36] John B. Pendry, D. Schurig, and David R. Smith. Controlling electromagnetic fields. *Science*, 312(5781):1780–1782, 2006.

[37] Howard DeVoe. Optical properties of molecular aggregates. ii. classical theory of the refraction, absorption, and optical activity of solutions and crystals. *The Journal of chemical physics*, 43:3199, 1965.

[38] Piotr J. Flatau and B.T. Draine. Discrete-dipole approximation for scattering calculations. *J. Opt. Soc. Am. A*, 11:1491, 1994.

[39] Maxim A. Yurkin and Alfons G. Hoekstra. The discrete dipole approximation: an overview and recent developments. *Journal of Quantitative Spectroscopy and Radiative Transfer*, 106(1):558–589, 2007.

[40] Leung Tsang, Jin Au Kong, Kung-Hau Ding, and Chi On Ao. *Scattering of electromagnetic waves, numerical simulations*, volume 25. Wiley. com, 2004.

[41] John D. Kraus. *Antennas for all applications.* New York: McGraw-Hill, 2002.

[42] Adesoji Sajuyigbe. Electromagnetic metamaterials for antenna applications. *Ph.D. dissertation*, Phys., Duke University, Durham, N.C., 2010.

[43] Constantine A. Balanis. *Antenna theory: analysis and design.* John Wiley & Sons, 2012.

[44] P. Checcacci, V. Russo, and A. Scheggi. Holographic antennas. *Antennas and Propagation, IEEE Transactions on*, 18(6):811–813, 1970.

[45] Winston E. Kock. Engineering applications of lasers and holography. *New York, Plenum Press, 1975. 414 p.*, 1, 1975.

[46] Moniem ElSherbiny, Aly E. Fathy, Arye Rosen, Gary Ayers, and Stewart M. Perlow. Holographic antenna concept, analysis, and parameters. *Antennas and Propagation, IEEE Transactions on*, 52(3):830–839, 2004.

[47] Alejandro Javier Martinez-Ros, Jose Luis Gomez-Tornero, and George Goussetis. Holographic pattern synthesis with modulated substrate integrated waveguide line-source leaky-wave antennas. *Antennas and Propagation, IEEE Transactions on*, 61(7):3466–3474, 2013.

[48] F. Caminita, M. Nannetti, and Stefano Maci. A design method for curvilinear strip grating holographic antennas. In *Antennas and Propagation Society International Symposium, 2008. AP-S 2008. IEEE*, pages 1–4. IEEE, 2008.

[49] Adrian Sutinjo, Michal Okoniewski, and Ronald H. Johnston. A holographic antenna approach for surface wave control in microstrip antenna applications. *Antennas and Propagation, IEEE Transactions on*, 58(3):675–682, 2010.

[50] Arthur A. Oliner and David R. Jackson. *Leaky-wave antennas*, volume 4. New York: McGraw-Hill, 1993.

[51] Paolo Burghignoli, Fabrizio Frezza, Alessandro Galli, and Giuseppe Schettini. Synthesis of broad-beam patterns through leaky-wave antennas with rectilinear geometry. *Antennas and Wireless Propagation Letters, IEEE*, 2(1):136–139, 2003.

[52] José Luis Gomez-Tornero, Alejandro Javier Martínez-Ros, and Rafael Verdu-Monedero. Fft synthesis of radiation patterns with wide nulls using tapered leaky-wave antennas. *Antennas and Wireless Propagation Letters, IEEE*, 9:518–521, 2010.

[53] M. Nannetti, F. Caminita, and Stefano Maci. Leaky-wave based interpretation of the radiation from holographic surfaces. In *Antennas and Propagation Society International Symposium, 2007*, pages 5813–5816. IEEE, 2007.

[54] Amit M. Patel and Anthony Grbic. A printed leaky-wave antenna based on a sinusoidally-modulated reactance surface. *Antennas and Propagation, IEEE Transactions on*, 59(6):2087–2096, 2011.

[55] Ladislau Matekovits, GC Vietti Colomé, and Mario Orefice. Controlling the bandlimits of te-surface wave propagation along a modulated microstrip-line-based high impedance surface. *Antennas and Propagation, IEEE Transactions on*, 56(8):2555–2562, 2008.

[56] Ladislau Matekovits. Analytically expressed dispersion diagram of unit cells for a novel type of holographic surface. *Antennas and Wireless Propagation Letters, IEEE*, 9:1251–1254, 2010.

[57] Arthur A. Oliner and Alexander Hessel. Guided waves on sinusoidally-modulated reactance surfaces. *Antennas and Propagation, IRE Transactions on*, 7(5):201–208, 1959.

[58] Dan Sievenpiper, James Schaffner, Robert Loo, Gregory Tangonan, Samuel Ontiveros, and Rick Harold. A tunable impedance surface performing as a reconfigurable beam steering reflector. *Antennas and Propagation, IEEE Transactions on*, 50(3):384–390, 2002.

[59] Bryan H. Fong, Joseph S. Colburn, John J. Ottusch, John L. Visher, and Daniel F. Sievenpiper. Scalar and tensor holographic artificial impedance surfaces. *Antennas and Propagation, IEEE Transactions on*, 58(10):3212–3221, 2010.

[60] Gabriele Minatti, Francesco Caminita, Massimiliano Casaletti, and Stefano Maci. Spiral leaky-wave antennas based on modulated surface impedance. *Antennas and Propagation, IEEE Transactions on*, 59(12):4436–4444, 2011.

[61] Gabriele Minatti, Stefano Maci, Paolo De Vita, Angelo Freni, and Marco Sabbadini. A circularly-polarized isoflux antenna based on anisotropic metasurface. *Antennas and Propagation, IEEE Transactions on*, 60(11):4998–5009, 2012.

[62] Symon K. Podilchak, Ladislau Matekovits, A.l.P Freundorfer, Karu Esselle, and Yahia M.M. Antar. Modulated strip-line leaky-wave antenna using a printed grating lens and a surface-wave source. In *Antenna Technology and Applied Electromagnetics & the American Electromagnetics Conference (ANTEM-AMEREM), 2010 14th International Symposium on*, pages 1–3. IEEE, 2010.

[63] S. Podilchak, Ladislau Matekovits, A. Freundorfer, Y Antar, and Mario Orefice. Controlled leaky-wave radiation from a planar configuration of width-modulated microstrip lines. *Antennas and Propagation, IEEE Transactions on*, pages 4957–4972, 2013.

[64] G.C. Taylor, S.M. Perlow, A. Rosen, A.E. Fathy, S. Kanamaluru, and M. Esherbiny. Reconfigurable antenna, May 20 2003. US Patent 6,567,046.

[65] Filippo Costa, Agostino Monorchio, Salvatore Talarico, and Fabio Michele Valeri. An active high-impedance surface for low-profile tunable and steerable antennas. *Antennas and Wireless Propagation Letters, IEEE*, 7:676–680, 2008.

[66] Daniel J. Gregoire, Joseph S. Colburn, Amit M. Patel, R. Quarfoth, and Daniel Sievenpiper. A low profile electronically-steerable artificial-impedance-surface antenna. In *Electromagnetics in Advanced Applications (ICEAA), 2014 International Conference on*, pages 477–479. IEEE, 2014.

[67] Ladislau Matekovits, M. Heimlich, and K.P. Esselle. Metamaterial-based millimeter-wave switchable leaky wave antennas for on-chip implementation in gaas technology. *Journal of Electromagnetic Waves and Applications*, 25(1):49–61, 2011.

[68] Ladislau Matekovits, Michale Heimlich, and Karu P. Esselle. Tunable periodic microstrip structure on gaas wafer. *Progress In Electromagnetics Research*, 97:1–10, 2009.

[69] C.L. Dolph. A current distribution for broadside arrays which optimizes the relationship between beam width and side-lobe level. *Proceedings of the IRE*, 34(6):335–348, 1946.

[70] R. Hansen. A one-parameter circular aperture distribution with narrow beamwidth and low sidelobes. *Antennas and Propagation, IEEE Transactions on*, 24(4):477–480, 1976.

[71] A.K.M. Baki, Naoki Shinohara, Hiroshi Matsumoto, Kozo Hashimoto, and Tomohiko Mitani. Study of isosceles trapezoidal edge tapered phased array antenna for solar power station/satellite. *IEICE transactions on communications*, 90(4):968–977, 2007.

[72] Robert J. Mailloux. *Phased array antenna handbook*. Artech House Boston, MA, 2005.

[73] Arun K. Bhattacharyya. *Phased array antennas: Floquet analysis, synthesis, BFNs and active array systems*, volume 179. John Wiley & Sons, 2006.

[74] Robert C. Hansen. *Phased array antennas*, volume 213. Wiley.com, 2009.

[75] P.W. Howells. Intermediate frequency side-lobe canceller, August 24 1965. US Patent 3,202,990.

[76] Dean D. Howard. Sidelobe cancelling system for array type target detectors, March 25 1969. US Patent 3,435,453.

[77] I.N. Durboraw. Clutter compensated sidelobe cancelling communications system, April 26 1983. US Patent 4,381,508.

[78] I. Tsujimoto. Sidelobe cancellation and diversity reception using a single array of auxiliary antennas, November 29 1994. US Patent 5,369,412.

[79] Bernard Widrow, John R. Glover Jr., John M. McCool, John Kaunitz, Charles S. Williams, Robert H. Hearn, James R. Zeidler, Eugene Dong Jr, and Robert C. Goodlin. Adaptive noise cancelling: Principles and applications. *Proceedings of the IEEE*, 63(12):1692–1716, 1975.

[80] C. Baird and G. Rassweiler. Adaptive sidelobe nulling using digitally controlled phase-shifters. *Antennas and Propagation, IEEE Transactions on*, 24(5):638–649, 1976.

[81] W.F. Frost, R.J. Masak, H.F. Baurle, and A.F. Kowalski. Multilevel sidelobe canceller, June 27 1978. US Patent 4,097,866.

[82] Lloyd J. Griffiths and Charles W. Jim. An alternative approach to linearly constrained adaptive beamforming. *Antennas and Propagation, IEEE Transactions on*, 30(1):27–34, 1982.

[83] Sven E. Nordholm and Yee Hong Leung. Performance limits of the broadband generalized sidelobe cancelling structure in an isotropic noise field. *The Journal of the Acoustical Society of America*, 107(2):1057–1060, 2000.

[84] W. Herbordt and W. Kellermann. Efficient frequency-domain realization of robust generalized sidelobe cancellers. In *IEEE Workshop on Multimedia Signal Processing*, pages 377–382, 2001.

[85] Parijat Oak and Walter Kellermann. A calibration algorithm for robust generalized sidelobe cancelling beamformers. In *Proc. Int. Workshop on Acoustic Echo and Noise Control (IWAENC)*, pages 97–100. Citeseer, 2005.

[86] J. Boyan and A. W Moore. Generalization in reinforcement learning: Safely approximating the value function. *Advances in neural information processing systems*, page 369376, 1995.

[87] Robert A. Monzingo and Thomas W. Miller. *Introduction to adaptive arrays*. SciTech Publishing, 1980.

[88] John Litva and Titus K. Lo. *Digital beamforming in wireless communications*. Artech House, Inc., 1996.

[89] Joseph C. Liberti and Theodore S. Rappaport. *Smart antennas for wireless communications: IS-95 and third generation CDMA applications*. Prentice Hall PTR, 1999.

[90] Harry L. Van Trees. *Detection, Estimation, and Modulation Theory, Optimum Array Processing*. John Wiley & Sons, 2004.

[91] H. Lebret and S. Boyd. Antenna array pattern synthesis via convex optimization. *Signal Processing, IEEE Transactions on*, 45(3):526–532, MAR 1997.

[92] R.T. Compton. *Adaptive antennas: concepts and performance*, volume 18. Prentice-Hall Englewood Cliffs, NJ, 1988.

[93] Michael Chryssomallis. Smart antennas. *Antennas and Propagation Magazine, IEEE*, 42(3):129–136, 2000.

[94] Simon Haykin. Array signal processing. *Englewood Cliffs, NJ, Prentice-Hall, Inc., 1985, 493 p. For individual items see A85-43961 to A85-43963.*, 1, 1985.

[95] Robert Schreiber. Implementation of adaptive array algorithms. *IEEE transactions on acoustics, speech, and signal processing*, 34:1038–1045, 1986.

[96] Fan Wang, Roy Yang, and Colin Frank. A new algorithm for array pattern synthesis using the recursive least squares method. *Signal Processing Letters, IEEE*, 10(8):235–238, 2003.

[97] S. Kazemi, Hamid Reza Hassani, Gholamreza R. Dadashzadeh, and Fatemeh Geran Gharakhili. Performance improvement in amplitude synthesis of unequally spaced array using least mean square method. *Progress In Electromagnetics Research B*, 1:135–145, 2008.

[98] E. Botha and D.A. McNamara. Conformal array synthesis using alternating projections, with maximal likelihood estimation used in one of the projection operators. *Electronics Letters*, 29(20):1733–1734, 1993.

[99] I. Chiba, W. Chujo, and M. Fujise. Beam space constant modulus algorithm adaptive array antennas. In *Antennas and Propagation, 1993., Eighth International Conference on*, pages 975–978. IET, 1993.

[100] Seungwon Choi and Tapan K. Sarkar. Adaptive antenna array utilizing the conjugate gradient method for multipath mobile communication. *Signal processing*, 29(3):319–333, 1992.

[101] Yahya Rahmat-Samii and Eric Michielssen. *Electromagnetic optimization by genetic algorithms*. John Wiley & Sons, Inc., 1999.

[102] Francisco J. Ares-Pena, Juan A. Rodriguez-Gonzalez, Emilio Villanueva-Lopez, and S.R. Rengarajan. Genetic algorithms in the design and optimization of antenna array patterns. *Antennas and Propagation, IEEE Transactions on*, 47(3):506–510, 1999.

[103] Randy L. Haupt. An introduction to genetic algorithms for electromagnetics. *Antennas and Propagation Magazine, IEEE*, 37(2):7–15, 1995.

[104] Daniel W. Boeringer and Douglas H. Werner. Particle swarm optimization versus genetic algorithms for phased array synthesis. *Antennas and Propagation, IEEE Transactions on*, 52(3):771–779, 2004.

[105] Majid M. Khodier and Christos G. Christodoulou. Linear array geometry synthesis with minimum sidelobe level and null control using particle swarm optimization. *Antennas and Propagation, IEEE Transactions on*, 53(8):2674–2679, 2005.

[106] Nanbo Jin and Yahya Rahmat-Samii. Advances in particle swarm optimization for antenna designs: Real-number, binary, single-objective and multiobjective implementations. *Antennas and Propagation, IEEE Transactions on*, 55(3):556–567, 2007.

[107] R.G. Ayestaran, F. Las-Heras, and J.A. Martinez. Non uniform-antenna array synthesis using neural networks. *Journal of Electromagnetic Waves and Applications*, 21(8):1001–1011, 2007.

[108] Saber Helmy Zainud-Deen, H.A. Malhat, Kamal Hassan Awadalla, and E.S. El-Hadad. Direction of arrival and state of polarization estimation using radial basis function neural network (rbfnn). In *Radio Science Conference, 2008. NRSC 2008*, pages 1–8. IEEE, 2008.

[109] R.G. Ayestaran, J. Laviada, and F. Las-Heras. Synthesis of passive-dipole arrays with a genetic-neural hybrid method. *Journal of Electromagnetic Waves and Applications*, 20(15):2123–2135, 2006.

[110] Kartik B. Ariyur and Miroslav Krstic. *Real-time optimization by extremum-seeking control*. John Wiley & Sons, 2003.

[111] Y. Tan, W.H. Moase, C. Manzie, D. Nesic, and I.M.Y. Mareels. Extremum seeking from 1922 to 2010. In *Control Conference (CCC), 2010 29th Chinese*, pages 14–26. IEEE, 2010.

[112] Paolo Binetti, Kartik B. Ariyur, Miroslav Krstic, and Franco Bernelli. Formation flight optimization using extremum seeking feedback. *Journal of Guidance, Control, and Dynamics*, 26(1):132–142, 2003.

[113] Andrzej Banaszuk, Kartik B. Ariyur, Miroslav Krstić, and Clas A. Jacobson. An adaptive algorithm for control of combustion instability. *Automatica*, 40(11):1965–1972, 2004.

[114] Steven L. Brunton, Clarence W. Rowley, Sanjeev R. Kulkarni, and Charles Clarkson. Maximum power point tracking for photovoltaic optimization using ripple-based extremum seeking control. *Power Electronics, IEEE Transactions on*, 25(10):2531–2540, 2010.

[115] C. Danielson, S. Lacy, B. Hindman, P. Collier, J. Hunt, and R. Moser. Extremum seeking control for simultaneous beam steering and wavefront correction. In *2006 American Control Conference (ACC)*, pages 596–601. IEEE, 2006.

[116] Miroslav Krstić and Hsin-Hsiung Wang. Stability of extremum seeking feedback for general nonlinear dynamic systems. *Automatica*, 36(4):595–601, 2000.

[117] Joon-Young Choi, Miroslav Krstic, Kartik B. Ariyur, and Jin Soo Lee. Extremum seeking control for discrete-time systems. *Automatic Control, IEEE Transactions on*, 47(2):318–323, 2002.

[118] Mikala Johnson, Patrick Bowen, Nathan Kundtz, and Adam Bily. Discrete-dipole approximation model for control and optimization of a holographic metamaterial antenna. *Applied Optics*, 53(25):5791–5799, 2014.

[119] J Nathan Kutz. *Data-driven modeling & scientific computation: methods for complex systems & big data*. Oxford University Press, 2013.

[120] C.G. Atkeson and J. Morimoto. Nonparametric representation of policies and value functions: A trajectory-based approach. *Advances in neural information processing systems*, page 16431650, 2003.

[121] Remi Munos and Andrew Moore. Variable resolution discretization for high-accuracy solutions of optimal control problems. In *Proceedings of the 16th international joint conference on Artificial intelligence - Volume 2*, pages 1348–1355, Stockholm, Sweden, 1999. Morgan Kaufmann Publishers Inc.

[122] Mingyuan Zhong, Mikala Johnson, Yuval Tassa, Tom Erez, and Emanuel Todorov. Value function approximation and model predictive control. In *Adaptive Dynamic Programming And Reinforcement Learning (ADPRL), 2013 IEEE Symposium on*, pages 100–107. IEEE, 2013.

[123] Christopher M. Bishop. *Pattern recognition and machine learning*, volume 1. springer New York, 2006.

[124] Emmanuel J. Candès. Compressive sampling. In *Proceedings oh the International Congress of Mathematicians: Madrid, August 22-30, 2006: invited lectures*, pages 1433–1452, 2006.

[125] Dongbin Xiu. Fast numerical methods for stochastic computations: a review. *Communications in computational physics*, 5(2-4):242–272, 2009.

Appendix A

METAMATERIAL ANTENNA MODELING

A.1 Coupling Coefficients

This appendix gives the derivation of the coupling coefficients between the incident field due to one cell and the resulting scattered field of another cell for the DDA model of a waveguide-fed array of resonators given in section 2.2.3.

First, the relationship between the electric fields at the ports in terms of the classical insertion loss scattering parameter, $S_{21}^{n,m}$ (see figure A.1:

$$\mathbf{E}_n^{tot}(\mathbf{x}_{P2}) = S_{21}^{n,m}\mathbf{E}_m^{tot}(\mathbf{x}_{P1}), \tag{A.1}$$

where $P1$ and $P2$ denote the measurement of the fields at ports 1 and 2 respectively.

Next, writing the field of the n-th mode at port 2 in relation to the scattered field of the unit cell:

$$\begin{aligned}\mathbf{E}_n^{tot}(\mathbf{x}_{P2}) &= \text{(propagating input field at port 1}\\ &\quad\ \text{measured at port 2)}\\ &+ \text{(forward scattered field of scatterer 1}\\ &\quad\ \text{measured at port 2).}\end{aligned}$$

The first term is just $\mathbf{E}_{P1,n}^{tot}(\mathbf{x}_{P2})$. The second term is $\mathbf{E}_{1,n^+}^{scatt}(\mathbf{x}_{P2})$ where the + denotes the forward scattered component.

Further, describing the field at port 1 as being the result of an effective forward scattered field from a cell upstream in the waveguide, cell number 0, $\mathbf{E}_{0,m^+}^{scatt}$, use equation (2.4) to obtain:

$$\mathbf{E}_{n^+}^{1,scatt} = \sum_{m=1}^{M} C_{1,0}^{n,m}\mathbf{E}_{m^+}^{0,scatt}(\mathbf{x}_1). \tag{A.2}$$

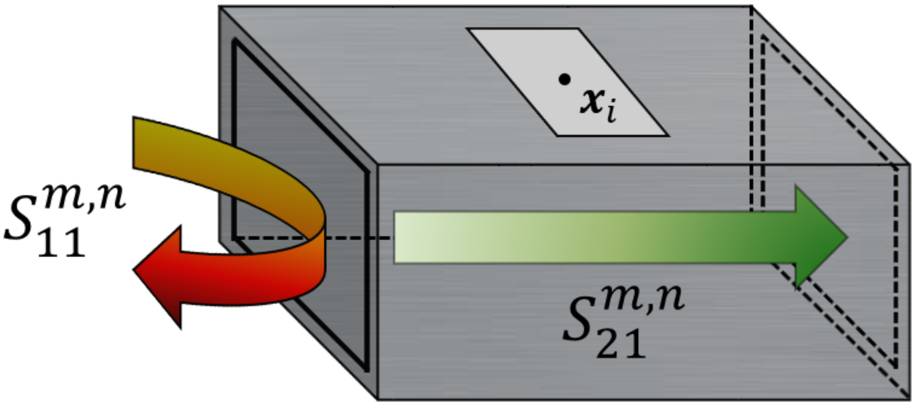

Figure A.1: Scattering parameters extracted from full-wave simulation of a single cell define the coupling coefficients of the DDA model.

Using equation (A.2) in equation(A.1),

$$\begin{aligned} \mathbf{E}_n^{tot}(\mathbf{x}_{P2}) &= S_{nm}^{21}\mathbf{E}_{P1,m}^{tot}(\mathbf{x}_1) \quad (A.3) \\ &= \mathbf{E}_{P1,n}^{tot}(\mathbf{x}_{P2}) \\ &\quad + \sum_{m=1}^{M} C_{1,0}^{n,m}\mathbf{E}_{m^+}^{0,scatt}(\mathbf{x}_1). \quad (A.4) \end{aligned}$$

Simplifying the above expressions and generalizing to any pair of cells $j > i$, the coupling coefficient is defined as:

$$C_{j,i}^{n,m} = S_{21}^{n,m} - \delta_{nm}. \quad (A.5)$$

This general equation must be used with careful attention to the location of the measurement of the fields, i.e. all field quantities in equations (A.4) must be de-embedded to a common location.

Now turn to the case of cells $j < i$, i.e. the upstream effect of a cell because of the cell's effect on the waveguide field. This backward coupling is derived from the return loss parameter, $S_{11}^{n,m}$:

$$\mathbf{E}_{n,out}^{tot}(\mathbf{x}_{P1}) = S_{11}^{n,m}\mathbf{E}_{m,in}^{tot}(\mathbf{x}_{P1}). \quad (A.6)$$

Replacing the total fields in equation (A.6) with the scattered field equivalents one obtains:

$$\mathbf{E}^{1,scatt}_{n^-}(\mathbf{x}_{P1}) = S^{n,m}_{11}\mathbf{E}^{0,scatt}_{m^+}(\mathbf{x}_{P1}), \tag{A.7}$$

where the $-$ refers to the backward propagating field.

Comparing this expression with the definition of the coupling coefficients in equation (2.4), the coupling coefficient for all cells $j < i$ is given by:

$$C^{n,m}_{j,i} = S^{n,m}_{11}, \tag{A.8}$$

where, once more, attention must be paid to the location of the measurement of the fields, i.e. all field quantities in equation (A.7) must be de-embedded to a common location.

A.2 Computational Methods

This appendix gives specifics of the two other commonly used models for prediction of the excitation of the meta-atoms as applied to the metamaterial antenna under consideration in this paper to which I compare the DDA model in section 2.3.

A.2.1 Array Factor

The simplest model which one might wish to use to predict the far-field radiation pattern of an array of resonators is a straightforward array factor model under the assumption of an ideal traveling surface wave phase distribution at the location of each resonator. In the DDA model, the complex excitation of each dipole is found by solution of the self-consistent DDA matrix system. If, instead, one neglects any possible shift in the phase from the underlying traveling wave, and one assumes some maximal and minimal amplitude of radiation, the polarizability of the dipoles is defined by:

$$\mathbf{P}_{j,m} = A\angle\text{feed} = A\exp(\mathbf{k}_m \cdot \mathbf{x}_j), \tag{A.9}$$

where A is the assumed amplitude and $\mathbf{k}_m$ is the wavevector of the m-th waveguide mode.

The assumption of no phase shifting by the scatterer is not true in the case of an impedance-induced resonance, and the assumption of fixed amplitudes of radiation everywhere in the array is not true in the case of resonators coupled to a waveguide field because the field decays by ohmic loss and, more pronouncedly, by the scattering of energy by upstream cells. However, to a zeroth order, these assumptions give the illuminating reference wave of the holographic pattern calculation, and are, therefore, acceptable simplifying idealizations which provides a very fast base-line model.

A.2.2 Circuit Equivalent

A circuit model includes the two effects of phase shift by the resonator and amplitude decay down the waveguide using a cascaded scattering approach. In the circuit model the behavior of the resonators is modeled as a general serial shunt impedance as indicated in figure A.2. The distance in the waveguide between resonators acts as a transmission line with an effective phase variation and dispersion, also shown in figure A.2.

The circuit equivalent cascades the effects from the input, through one resonator, through a small transmission line, to another resonator, to another transmission line, and so forth until reaching the end of the waveguide. In this way, the upstream phase variations and field decay are correctly accounted for at a downstream cell. Note that definition of the impedance on a cell-by-cell basis is amenable to handling the case of individually tuned resonators as is requisite for holographic beamforming.

The important effect that is not captured by the circuit equivalent but that is captured by the DDA model is the backward propagating effects (see the discussion of the coupling coefficient derivation in section 2.2.3). The simultaneous solve of the DDA resolves all the pairwise interactions between cells where the circuit model only accounts for the compounded upstream effects.

Note that one can extract the R, L, and C parameters which define the impedance from test or full-wave simulation in a manner analogous to the extraction of the coupling coefficients for the DDA model. Then the complex excitation of a cell is the difference

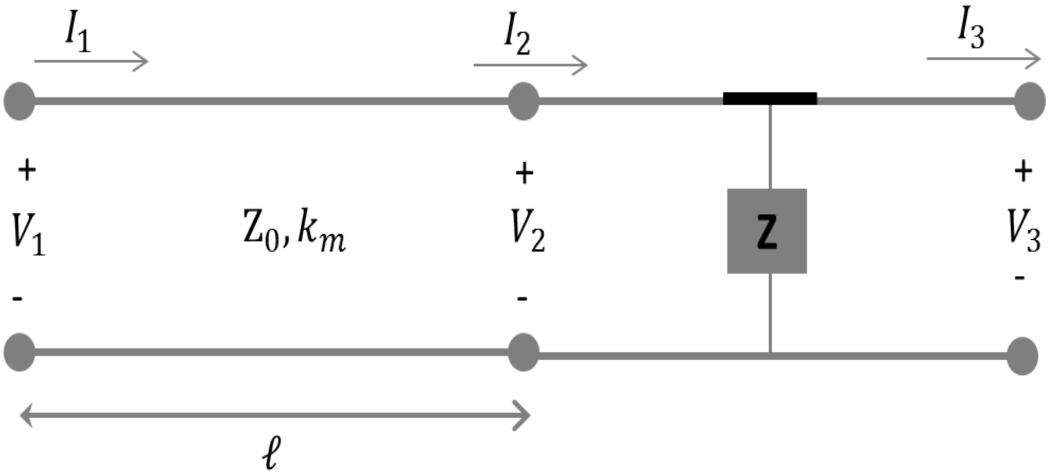

Figure A.2: Circuit equivalent of a metamaterial antenna unit cell with transmission line between cells and shunt impedance representing meta-atom resonant response.

between the current on the downstream side of a cell and the current on the upstream side.